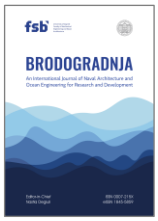
Brodogradnja Volume 78 Number 1 (2027) 78108

University of Zagreb
Faculty of Mechanical
Engineering and Naval
Architecture

journal homepage: www.brodogradnja.fsb.hr

Brodogradnja

An International Journal of Naval Architecture and
Ocean Engineering for Research and Development



Analysis of turning maneuverability performance of a tanker in shallow water under wind disturbances

Islam Mohamed Sherif [1,2,3], *Ping Xin* [1,3], *Xueqian Zhou* [1,3*]

[1]*College of Shipbuilding Engineering, Harbin Engineering University, Harbin, Heilongjiang, China*
[2]*College of Fish Resources and Marine Studies, Suez University, Suez, Egypt*
[3]*International Joint Laboratory of Naval Architecture and Offshore Technology, Harbin, China*

ARTICLE INFO

Keywords:
Maneuvering performance
Wind force
MMG model
Shallow water
Turning maneuvering

ABSTRACT

Increasing ship dimensions and maritime traffic have intensified maneuvering challenges in harbors and channels, particularly in shallow water under external wind disturbances. This study investigates the effects of steady wind on ship turning performance using a Maneuvering Modeling Group (MMG) model incorporating regression-based aerodynamic coefficients. Simulations are conducted across different ship speeds, depth-to-draft ratios (h/T), wind speeds, and wind directions. The model is validated qualitatively and quantitatively against experimental turning data in deep and shallow water. Turning performance is assessed through trajectories, advance, transfer, yaw rate, drift angle, and forward speed. The results indicate that, at 75 % of full ship speed, winds exceeding 5 m/s can either elongate or contract turning trajectories, depending on wind conditions. Wind-induced trajectory changes are more pronounced at h/T=1.2 and generally diminish with increasing water depth. Yaw-rate magnitude shows greater wind sensitivity at h/T=1.2, whereas drift-angle magnitude is more affected at h/T=3. Headwinds produce the largest reduction in forward speed, particularly at h/T=3 and reduced ship speed. Sensitivity analysis of input and output variables indicates that their relationships are nonlinear (non-monotonic), except for the h/T ratio. Finally, drift angle shows the greatest variability among the investigated scenarios.

1. Introduction

As the volume of commercial maritime transportation through coastal areas, waterways, and channels continues to increase, for instance, in Panama, the St. Lawrence waterway, and the Suez Canal, which are among the most heavily used, the probability of maritime accidents, including collisions, blockages, contact, and groundings, also rises. Therefore, ships must take greater precautions and remain more aware when maneuvering in shallow water. Maneuvering becomes even more challenging when combined with external disturbances such as wind, waves, water currents, and bank-interaction effects. In the case of wind, the situation becomes critical for two reasons. First, hydrodynamic interaction affects the ship's wetted surface

* Corresponding author.
E-mail address: xueqian.zhou@hrbeu.edu.cn

https://doi.org/10.21278/brod78108
Received 27 April 2026; Received in revised form 24 October 2026; Accepted 25 October 2026
Available online 11 November 2026
ISSN 0007-215X; eISSN 1845-5859

due to viscous effects and bottom restrictions; second, aerodynamic forces act on the superstructures due to wind disturbances. These combined effects significantly influence ship maneuvering performance.

Numerous researchers have investigated ship maneuvering in shallow water; for instance, Kim et al. [1] examined the impact of waves on the maneuvering performance of a KRISO container ship using CFD by solving the URANS model. Based on URANS, the added resistance in short regular waves [2] and the scale effects of viscous roll damping [3] have been studied. Atasayan et al. [4] predicted the zigzag maneuvering performance of a tanker using an offline grey box method. El Moctar et al. [5] studied maneuvering performance in calm water and waves through model tests and numerical simulations for a container and a tanker, solving the Reynolds-Averaged Navier-Stokes (RANS) equations. Hasnan et al. [6] investigated ship turning in regular waves using a free-running model test. Their analysis, based on the linear Nomoto model, showed satisfactory prediction of drift induced by wave action. Investigating these external influences on ship maneuvering behavior provides mariners and captains with valuable safety insights to help avoid potential issues under complex operational conditions. The recommendation by Sutulo and Guedes Soares [7] further confirmed the importance of studying the influence of wind on ship maneuvering behavior.

One of the most recent shallow water incidents that attracted global attention was the blockage of the Suez Canal by the container ship MV EVERGIVEN, as shown in Figure 1. This incident highlighted the complexity of ship maneuvering in restricted waterways, where grounding, collisions, and blockages may result from the combined effects of vessel characteristics, environmental conditions, navigation conditions, and operational factors. Wind effects were among the environmental factors discussed in relation to the maneuvering challenges experienced during the incident [8]. Therefore, understanding how wind forces affect ship maneuvering performance is essential for evaluating vessel behavior under various operational conditions, particularly for large ships operating in confined waters. However, studies on maneuver prediction that account for environmental disturbances in coastal areas and restricted waterways remain limited [9].

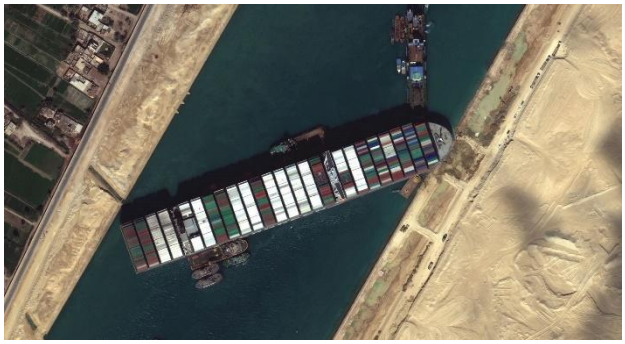


Fig. 1 Blockage of the Suez Canal by the EVERGIVEN container ship. (March, 2021)

The assessment of maneuvering trajectories and indices is important from a navigational safety perspective. Ship maneuvering performance with/without accounting for external disturbances has been widely studied using the MMG and Abkowitz models. Regarding system-based approaches, Du et al. [10] studied ship maneuvering on the Esso Bernicia tanker in a confined waterway using a nonlinear model and an optimization technique to estimate optimal hydrodynamic coefficients, which were then used to predict ship maneuvering. Gadelho et al. [11] numerically identified the hydrodynamic coefficients at various sections of the S175 hull model using a time-domain CFD model in both deep and shallow water. Liu et al. [12] predicted ship maneuvering in deep and shallow water using a system-based empirical method for the KCS and DTC container models, based on the MMG model. Li et al. [13] studied turning and zigzag maneuvers of the KVLCC2 model using CFD with an overset-grid technique. Their results demonstrated that turning capability was worse under low depth-to-draft ratios. Carrica et al. [14] studied the 20/5 zigzag maneuver numerically and experimentally for the KCS model, showing satisfactory agreement between EFD and CFD, except for yaw and yaw rate, where the errors exceeded 15 %. Kim et al. [15] examined the sensitivity of hydrodynamic derivatives at low speeds for the KVLCC2 model using the Abkowitz modular mathematical model. They showed that these derivatives are more sensitive to zigzag maneuvers than to turning maneuvers.

Based on an empirical modular maneuver model, Inoue et al. [16] predicted maneuvering forces and moments using the hydrodynamic coefficients. Wang et al. [17] predicted ship maneuvering under the combined effect of waves, wind, and currents in 3-DOF in deep water. Sukas et al. [18] developed the MANSIM code to predict ship maneuvering in deep water using a 3-DOF modular mathematical model. Their results ascertained a nonlinear relationship between hydrodynamic derivatives and maneuvering indices. Taimuri et al. [19] developed a 6-DOF model to investigate the ONRT benchmark ship, considering the influence of regular wave and shallow water corrections obtained from circular motion tests. The results confirm that the proposed method can predict maneuvering trajectories for current and future vessel designs and determine the necessary evasive velocity to mitigate grounding risk. Kostoulas et al. [20] evaluated maneuvering performance in 4-DOF using time-domain simulations based on the Son and Nomoto model in deep and shallow water. Tang et al. [21] developed a numerical model for ship maneuvering that accounts for shallow water effects, using the fourth-order Runge–Kutta method. Their results showed that shallow-water effects increase ship resistance and reduce maneuverability. Novaselic et al. [22] investigated the effect of wind forces on the turning maneuver of a Ro-Ro ship model in deep water. The results provide an improved understanding of vessel trajectories and reveal that vessels may, in some cases, exhibit unexpected responses.

More recently, researchers have applied identification methods to ship maneuvering models. Zhu et al. [23] presented a deterministic 3-DOF model based on the Abkowitz model and the Support Vector Machine (SVM) identification method to analyze the impact of wind forces on the hydrodynamic coefficients in deep water. Their results showed the method's effectiveness for scenarios with wind speeds not exceeding 8 m/s and measurement noise below 13 %. Wang et al. [24] used a similar approach across varying perturbation levels; their results showed that models identified under mild and moderate environmental conditions yielded deviations below 10 %, which is deemed acceptable. As the perturbation level increases, the fidelity of the identified model decreases. Using Automatic Identification System (AIS) data, Huang et al. [25] evaluated maneuvering risks at the port entrance and inner traffic lanes. Zhu [26] applied a hybrid optimization algorithm to improve the prediction of maneuvering coefficients under wind disturbances. Yasukawa et al. [27] studied a pure car carrier vessel operating under steady wind conditions. The results demonstrated that course instability is mainly caused by aerodynamic derivatives that modify the yaw-restoring forces under the head and following wind conditions.

Most previous studies have investigated the hydrodynamic and aerodynamic forces on ships maneuvering separately. While several studies have focused on wave effects and some on wind effects in deep water, research on the combined influence of wind and shallow water on maneuvering performance, in terms of maneuvering indices, remains limited. This is critical, as the growing dimensions of modern vessels, combined with increasing traffic in shallow harbors and channels, demand a more comprehensive understanding of maneuvering behavior for various ship types under environmental disturbances. To address this gap, the present study provides a detailed investigation of the turning maneuver performance of the KVLCC2 benchmark hull under the combined effects of wind forces and shallow water conditions, using the MMG model. The KVLCC2 is selected as a representative hull type that serves as a benchmark in SIMMAN workshops and MASHCON conferences. The present study assumes steady wind conditions. Therefore, the aerodynamic forces are calculated from prescribed wind scenarios and are not updated according to the instantaneous ship velocity or heading. Consequently, the model is interpreted as a one-way wind-disturbed MMG model. The contributions of this study are summarized as follows:

(1) A 3-DOF MMG maneuvering model is established incorporating shallow water corrections for hydrodynamic coefficients, added mass, resistance, propeller, and rudder effects.

(2) Aerodynamic forces and yaw moment obtained using regression-based aerodynamic coefficients are incorporated as prescribed external disturbances, enabling assessment of wind-induced changes in turning performance under different water-depth conditions.

(3) A systematic parametric analysis is conducted to quantify the influence of wind speed, wind direction, ship speed, and depth-to-draft ratio (h/T) on turning maneuver characteristics.

(4) Analyzing the sensitivity of indices relevant to input variables and estimating the variability of various indices across wide operational conditions.

The remainder of the article is structured as follows: Section 2 describes the problem statement and methodology for establishing the maneuvering mathematical model. Section 3 presents the validation of the maneuvering model. Section 4 presents the results and analysis of simulation scenarios. Section 5 presents the sensitivity and variability analysis for the input and output parameters. Finally, the conclusion is presented in Section 6.

2. Problem statement

The turning maneuver under wind disturbances at different depth-to-draft ratios (*h/T*) is investigated using the MMG mathematical model. The aerodynamic force and moment coefficients are calculated over a range of wind angles from 0° to 180°. These forces are used as inputs to the mathematical model. The simulation scenarios include two directions: when the wind acts in the same direction as the ship turns, and when it acts in the opposite direction.

The turning trajectory, including maximum advance and transfer, yaw rate, drift angle, and forward speed changes, is then analyzed in both directions. Moreover, the sensitivity and variability of input and output maneuvering parameters are evaluated. The turning maneuver is simulated at 15° intervals to capture variations in trajectories and maneuvering indices accurately. For clarity, the wind scenarios are presented at 45° intervals, including headwind, oblique headwind, beam wind, aft quartering wind, and following wind.

2.1 Coordinate system definitions

To analyze the ship maneuvering problem under combined wind and shallow-water effects for the KVLCC2 model, a 3-DOF MMG-based maneuvering model is employed in the horizontal plane [28]. Two right-hand coordinate frames are used, as shown in Figure 2. An inertial fixed coordinate frame (Earth coordinate), o_0–$x_0y_0z_0$, has a pivot point centered at (O_0), and its plane represents the still water surface. ψ_w, and ψ_{aw} are true and apparent wind angles, respectively, as shown in the angles from the x_0 axis;U_w,U_{aw} are the true and apparent wind velocities, and the angle of ship heading is referred to as ψ. The ship's fixed coordinate frame is a moving frame fixed to the hull, with its origin at midship. The plane *xoy* coincides with the still water surface with the *xyz* axes, and the *x*, *y*, and *z* axes are located at the bow, starboard side, and vertically directed downward, respectively. Moreover, r, β, and δ_R are the yaw rate, drift angle, and rudder angle, respectively. u and v are the ship surge and sway velocities, respectively, which are used to estimate ship speed U, where $U=\sqrt{u^2+v^2}$. Figure 3 shows the schematic view of the scenarios investigated. These scenarios are investigated in two directions: when the wind acts in the same direction as the ship turns and in the opposite direction, at various wind angles.

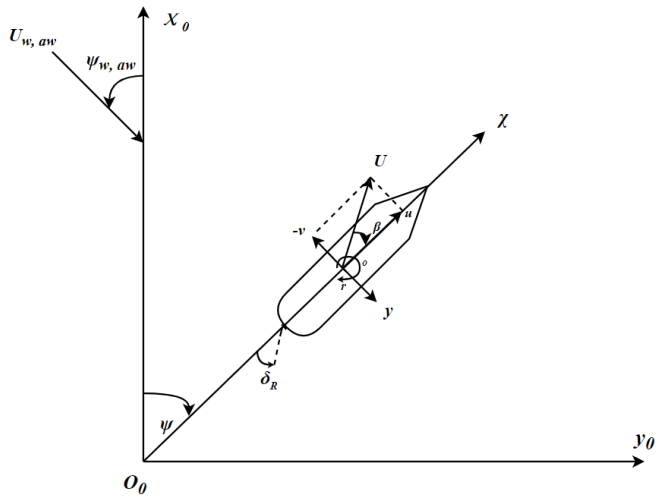


Fig. 2 Definition of coordinate systems

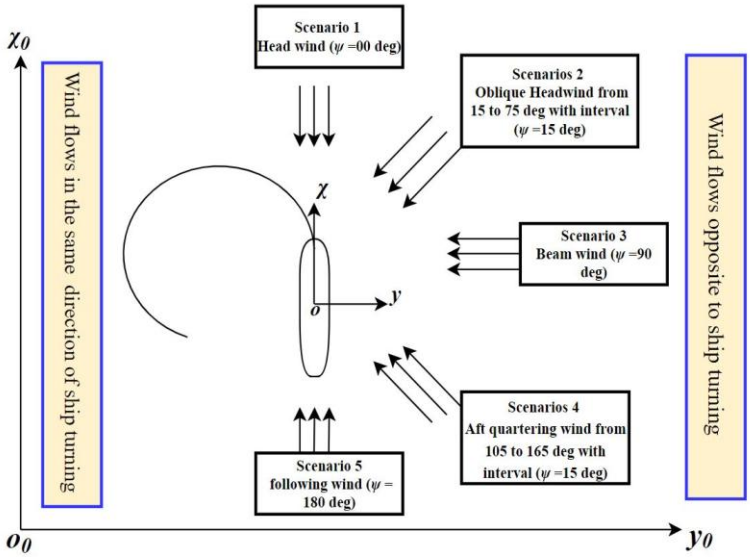


Fig. 3 Schematic view of the simulation scenarios

2.2 Equations of motion

The equations of motion form the core of the maneuvering model, which were established based on Newton's second law for a rigid body. The 3-DOF (surge, sway, and yaw) ship maneuvering motion can be expressed as:

$$\begin{aligned}
&\left(m+\mu_{11}\right)\dot{u}-m\left(vr+x_G r^2\right)=X_{\mathrm{H}}+X_{\mathrm{R}}+X_{\mathrm{P}}+X_{\mathrm{E}}\\
&\left(m+\mu_{22}\right)\dot{v}+mru+\left(mx_G+\mu_{26}\right)\dot{r}=Y_{\mathrm{H}}+Y_{\mathrm{R}}+Y_{\mathrm{E}}\\
&\left(I_{zz}+mx_{\mathrm{G}}^2+\mu_{66}\right)\dot{r}+(mx_{\mathrm{G}}+\mu_{62})\dot{v}+mx_{\mathrm{G}}ur=N_{\mathrm{H}}+N_{\mathrm{R}}+N_{\mathrm{E}}
\end{aligned} \tag{1}$$

where m is the ship mass, I_{zz} is the moment of inertia, x_G is the longitudinal coordinate of the center of gravity, $\dot{u},\dot{v}$ are the surge and sway accelerations in the x and y directions, respectively, and $\dot{r}$ is the yaw angular acceleration. The ship velocities are u and v in the x and y axes, and r is the yaw rate. $\mu_{11},\mu_{22},\mu_{66},\mu_{62},\mu_{26}$ are the added mass. On the right-hand side, the surge, sway forces, and yaw moments are denoted by X, Y, and N, respectively. The subscripts H, P, R, and E stand for the hull, propeller, rudder, and external forces, and X_{E}, Y_{E}, and N_{E} are the wind forces.

2.3 Hydrodynamic coefficients of a hull

The hydrodynamic coefficients are determined using existing formulas in the literature that have been extensively validated for maneuvering trajectory and its indices in both deep and shallow water. The equations for the added masses and moment components that explain the influence of the external forces on ship acceleration are determined as per Brix [29] and Clarke et al. [30].

The hydrodynamic forces and moments of the hull are expressed as follows:

$$\begin{aligned}
&X_H=0.5\rho LTU^2X'_H(v',r'),\\
&Y_H=0.5\rho LTU^2Y'_H(v',r'),\\
&N_H=0.5\rho L^2TU^2N'_H(v',r')
\end{aligned} \tag{2}$$

where ρ is the density of the fluid, L is the length of the ship, and T is the ship draft, $r'=rL/U$ is the non-dimensional yaw rate, and $v'=v/U$ is the non-dimensional sway velocity. The force and moment coefficients in a horizontal plane X'_H,Y'_H,N'_H are expressed as follows:

$$\begin{aligned}
&X'_H(v',r')=-R'_0+X'_{vv}v'^2+X'_{vr}v'r'+X'_{rr}r'^2+X'_{vvvv}v'^4\\
&Y'_H(v',r')=Y'_vv'+Y'_rr'+Y'_{vvv}v'^3+Y'_{vvr}v'^2r'+Y'_{vrr}v'r'^2+Y'_{rrr}r'^3
\end{aligned} \tag{3}$$

where R_0' is the ship resistance, estimated using Raven's method [31], as recommended by ITTC [32]. The hydrodynamic derivatives are calculated using existing empirical formulas, which $X'_{vvv}, X'_{vv}, X'_{rr}$, and N'_{rrr} are estimated as per Yoshimura and Masumoto [33]; $X'_{vr}, Y'_{vvv}, Y'_{rrr}$, and N'_{vvv} are calculated as per Lee and Shin [34]; Y'_v and N'_v are estimated according to Clarke et al. [30]; $Y'_{vvr}, Y'_{vrr}, N'_{vvr}$, and N'_{vrr} are calculated according to Kijima et al. [35]; Y'_r、is calculated as per Norrbin [36], and N'_r is estimated as per Khattab [37]. The first and third-order polynomial derivatives in Equation (3) provide superior estimation accuracy compared with the first and second-order polynomials for Y'_H and N'_H [28]. The shallow water correction factors for hydrodynamic derivatives, added mass, and the ship resistance coefficient are estimated according to [32, 35, 38-40] (see Appendix A and B).

The ship resistance is estimated by:

$$R_0 = 0.5\rho U^2 S_{\mathrm{W}} C_{\mathrm{T}} \tag{4}$$

where S_{W} is the wetted surface area of the hull and C_{T} is the drag coefficient. The C_{T} coefficient is dynamically evaluated from the instantaneous ship velocity.

$$C_{\mathrm{T}} = 1.06C_{\mathrm{F}}\left(1+k\right) + C_{\mathrm{w}} + \Delta C_{\mathrm{F}} \tag{5}$$

where C_{F} is the coefficient of frictional resistance on the hull surface, $\left(1+k\right)$ is the form factor, and C_{w} is the wave resistance coefficient.

$$C_{\mathrm{F}} = \frac{0.075}{\left(\log_{10} Re - 2\right)^2} \tag{6}$$

$$\left(1+k\right) = 1.017 + 20C_{\mathrm{B}}\left(B/L_{\mathrm{pp}}\right)^2\sqrt{T/B} \tag{7}$$

The drag coefficient caused by the roughness of the ship is:

$$\Delta C_{\mathrm{F}} = 0.044\left[\left(\frac{k_{\mathrm{s}}}{L_{\mathrm{pp}}}\right) - 10Re^{-\frac{1}{3}}\right] + 0.000125 \tag{8}$$

The empirical formula for shallow water correction on ship resistance is:

$$\frac{C_{T\,shallow}}{C_{T\,deep}} = 1 + 0.57\left(\frac{T}{h}\right)^{1.79} \tag{9}$$

where C_T is the viscous resistance coefficient; T and h are the ship draft and water depth, respectively. In this study, the fourth-order Runge-Kutta method is used to solve the time-domain equations of ship maneuvering motion.

2.4 Propeller force

The surge force as a result of the rotation of the propeller is estimated as:

$$X_P = (1-t_p)\rho n_p^2 D_P^4 K_T(J_P) \tag{10}$$

where t_p is the thrust deduction factor, n_p is the propeller rotation frequency, and D_P is the propeller diameter. The propeller thrust coefficient K_T is approximated as:

$$K_T(J_P) = k_2 J_P^2 + k_1 J_P + k_0 \tag{11}$$

where k_2, k_1, k_0 are the approximating coefficients, and J_P is the advance ratio:

$$J_P = \frac{u(1-w_p)}{n_p D_P} \tag{12}$$

where w_p is the wake fraction.

2.5 Rudder forces

The hydrodynamic forces induced by the rudder can be expressed as:

$$\begin{aligned} X_R &= -(1-t_R)F_N \sin\delta_R \\ Y_R &= -(1+a_H)F_N \cos\delta_R \\ N_R &= -(x_R + a_H x_H)F_N \cos\delta_R \end{aligned} \tag{13}$$

where δ_R is the rudder angle, t_R is the reduction factor of steering resistance, a_H is the rudder force increase coefficient, x_R and x_H are the longitudinal references of the rudder location and the acting point of additional sway force, respectively. The rudder normal force (F_N) is calculated according to Yasukawa and Yoshimura [28]. The rudder normal force F_N is:

$$F_N = 0.5\rho A_R U_R^2 f_a \sin\alpha_R \tag{14}$$

where A_R is the rudder area, f_a is the rudder lift gradient coefficient, α_R is the attack angle, U_R is the rudder velocity with respect to the rudder, where $U_R = \sqrt{u_R^2 + v_R^2}$, and the rudder surge force is given by:

$$u_R = \varepsilon u(1-w_P)\sqrt{\eta\left\{1+\kappa\left(\sqrt{1+\frac{8K_T}{\pi J_P^2}}-1\right)\right\}^2 + (1-\eta)}, \tag{15}$$

and the sway velocity of the rudder is estimated by:

$$v_R = U\gamma_R\beta_R \tag{16}$$

where η is the ratio of propeller diameter to rudder span, ε is the ratio of wake fraction for the propeller and rudder position, γ_R is the flow straightening coefficient, κ is an empirical constant, β_R is the effective rudder inflow angle in maneuvering motion. The shallow water effect on $t_p, \kappa, \gamma_R, w_P$ is estimated according to Amin and Hasegawa [41] (see Appendix C).

2.6 Aerodynamic forces

Various regression-based formulae have been developed to calculate the aerodynamic force on the ship. In this study, the aerodynamic coefficients are calculated using the method of Fujiwara et al. [42]. This method relies on the ship's form parameter and was developed through a regression analysis of various wind-tunnel experiments. The advantage of this method is that its standard error is smaller than that of other developed regression-based methods [42]. Furthermore, such methods are recommended by ITTC [43] for use when experimental work is unavailable. The longitudinal, transverse, and yawing coefficients are calculated for the KVLCC2 model, as shown in Figure 4. The forces and moments are then estimated and considered as external disturbances in the maneuvering model.

The aerodynamic forces and moments are expressed as:

$$\begin{aligned} X_E &= 0.5\rho_A U_{aw}^2 A_F C_X (X_0 + X_1\cos\psi_{aw} + X_3\cos 3\psi_{aw} + X_5\cos 5\psi_{aw}) \\ Y_E &= 0.5\rho_A U_{aw}^2 A_L C_Y (Y_1\sin\psi_{aw} + Y_3\sin 3\psi_{aw} + Y_5\sin 5\psi_{aw}) \\ N_E &= 0.5\rho_A U_{aw}^2 A_L L_{OA} C_N (N_1\sin\psi_{aw} + N_2\sin 2\psi_{aw} + N_3\sin 3\psi_{aw}) \end{aligned} \tag{17}$$

where C_X, C_Y, and C_N are the longitudinal, transverse, and moment coefficients; X_E, Y_E, and N_E are the calculated longitudinal, transverse forces, and yaw moments, respectively. ρ_A is the air density, and U_{aw} is the wind speed. A_L, A_F, and L_OA represent the lateral and frontal projected areas and the ship's length overall, respectively. $X_0, X_1, X_3, X_5, Y_1, Y_3, Y_5, N_1, N_2, N_3$ are the regression parameters.

In the time-domain implementation, the aerodynamic forces are pre-calculated for each prescribed steady wind condition and are then applied as constant external disturbances throughout the corresponding

maneuvering simulation. These aerodynamic forces are not dynamically recalculated during the time-domain integration. Therefore, changes in the instantaneous ship heading and velocity during the turning maneuver do not update the aerodynamic forces. The true and apparent wind quantities associated with the prescribed wind conditions are defined in Equations (18)-(22).

The true wind velocity vector in the Earth-fixed frame is:

$$V_{w_{(E)}} = \begin{bmatrix} -U_w \cos\psi_w \\ -U_w \sin\psi_w \end{bmatrix} \tag{18}$$

where U_w is the true wind speed and ψ_w is the true wind direction measured from the Earth-fixed x-axis; the negative signs in Equation (18) indicate that the true wind velocity vector points opposite to the wind-source direction, which represents a headwind velocity vector pointing aft (from bow to stern). Since the initial ship heading is 0° in all simulations, true wind angles of ψ_w=0°, 90°, and 180° correspond to headwind, starboard beam wind, and following wind, respectively. The ship's velocity in the Earth-fixed coordinate system is:

$$V_{s_{(E)}} = \begin{bmatrix} u\cos\psi - v\sin\psi \\ u\sin\psi + v\cos\psi \end{bmatrix} \tag{19}$$

where u is the surge velocity, v is the sway velocity, and ψ is the heading angle. The apparent wind velocity vector in the Earth-fixed coordinate system is:

$$\begin{aligned} V_{aw_{(E)}} &= V_{w_{(E)}} - V_{s_{(E)}} \\ V_{aw_{(E)}} &= \begin{bmatrix} -U_w \cos\psi_w - (u\cos\psi - v\sin\psi) \\ -U_w \sin\psi_w - (u\sin\psi + v\cos\psi) \end{bmatrix} \end{aligned} \tag{20}$$

Transforming the vector in Equation (20) into the ship's body-fixed coordinate (where the x-axis points forward and the y-axis points to starboard) yields:

$$\begin{aligned} R(\psi) &= \begin{bmatrix} \cos\psi & \sin\psi \\ -\sin\psi & \cos\psi \end{bmatrix} \\ V_{aw} &= \begin{bmatrix} V_{aw,(x)} \\ V_{aw,(y)} \end{bmatrix} = \begin{bmatrix} \cos\psi & \sin\psi \\ -\sin\psi & \cos\psi \end{bmatrix} \begin{bmatrix} V_{aw_{(E)},x} \\ V_{aw_{(E)},y} \end{bmatrix} \end{aligned} \tag{21}$$

Based on the above equations, the apparent wind speed and angle relative to the ship are expressed as:

$$\begin{aligned} U_{aw} &= \sqrt{(V_{aw_{(x)}})^2 + (V_{aw_{(y)}})^2} \\ \psi_{aw} &= a\tan 2(-V_{aw_{(y)}}, -V_{aw_{(x)}}) \end{aligned} \tag{22}$$

In Equation (22), the negative signs applied to the apparent wind velocity components represent the direction from which the apparent wind approaches, measured relative to the ship's bow. The apparent wind angle ψ_{aw} is calculated from the relative wind velocity and therefore depends on both the true wind velocity and the ship's velocity. Consequently, the apparent wind angle differs from the prescribed true wind angle. The calculated angle is used to evaluate the aerodynamic coefficients in Equation (17), following the angular reference and port-starboard sign convention of the adopted Fujiwara formulation.

For each prescribed wind scenario, the apparent wind angle is calculated once using the initial ship heading and initial velocity components according to Equations (18)-(22). The corresponding aerodynamic forces are then determined and held constant throughout that simulation. During time-domain integration, the instantaneous ship heading and velocity are not used to update the apparent wind direction and aerodynamic forces during the simulation. Consequently, the model represents a one-way wind-disturbed MMG model rather than a fully time-varying aero-hydrodynamic coupling. Table 1 presents the numerical implementation parameters and initial conditions used in the time-domain simulations. The sensitivity of the time-domain code is tested with several time steps; errors are less than 1 %; therefore, a time step of 0.1 is adopted.

Table 1 Numerical implementation parameters

Parameter	Value
Integration method	4th-order Runge–Kutta
Time step (Δt)	0.1s
Time-step sensitivity check	0.2, 0.1, 0.05 s (differences < 1 %)
Simulation duration	4000 s
Commanded rudder angle	35° port
Rudder rate	2.32 °/s
Rudder saturation	35°
Time to reach maximum rudder	15.09 s
Rudder execution	Applied at t=0
Initial sway velocity	0 m/s
Initial yaw rate	0 °/s
Initial heading	0°

3. Validation of maneuvering model

Two turning maneuvers are conducted for the KVLCC2 model in calm water, both in deep and shallow water. The maneuvering modular model is compared with experimental measurements conducted under both deep and shallow water conditions. For the deep water validation case, experiments were performed using a scale model with a geometric scale ratio of 45.714. The model was tested at an initial speed of 1.18 m/s, corresponding to a Froude number of 0.142 and an equivalent full-scale vessel speed of 15.5 knots. The maneuvering tests were conducted with a model-scale rudder rate of 15.68 °/s, while the water depth was maintained at 7.963 m. For the shallow water validation case, experimental tests were carried out using a model with a geometric scale ratio of 75.0. The model was operated at an initial speed of 0.415 m/s, corresponding to a Froude number of 0.064 and an equivalent full-scale vessel speed of 7 knots. The rudder rate was maintained at 15.68 °/s on the model scale, and the water depth was set to 0.3324 m. These experimental cases were selected as validation benchmarks to assess the established maneuvering model's capability to predict ship maneuvering behavior under different water-depth conditions. The validation uses a full-scale model, with an initial ship velocity of U_0 = 15.5 kn (7.973 m/s) in deep water and 7 kn (3.60 m/s) in shallow water, with a rudder rate of 2.32 °/s. The model tests used for validation purposes in deep and shallow water are presented in SIMMAN [44]. Table 2 displays the ship particulars of the KVLCC2 model, and Figure 5 shows its profile and body plan.

3.1 Validation for deep water

Figure 6 shows the turning maneuver trajectory at 35° port side and its indices, including yaw rate, drift angle, and speed change in deep water. The deep-water maneuvering performance is validated against the FRMT experimental benchmark as shown in Table 3. The numerical results show satisfactory agreement with the experimental measurements. The relative errors for the maneuvering indices remain below 10 %, with errors of 5.5 %, 4.8 %, and 2.3 % for advance, transfer, and tactical diameter, respectively. The yaw rate is predicted with a relative error of 1.4 %, while the speed change and drift angle show errors of 17.2 % and 4.3 %, respectively. The large relative error percentage of speed change between the experimental and numerical results may be due to the empirical resistance formulation and differences in the damping ratio and viscous effects arising from the different scale models. Despite this deviation in the speed magnitude, the model adequately captures the qualitative evolution of the speed during the maneuver.

Table 2 Ship particulars of the KVLCC2 model

Parameters	Symbol (Units)	Value
Scale	λ	1.00
Ship Length	L_{PP} (m)	320.0
Length overall	L_{OA}(m)	325.5
Breadth	B (m)	58.0
Displacement volume	∇ (m^3)	312600
Longitudinal gravity center	x_G (m)	11.2
Draft	T (m)	20.8
Block coefficient	C_B	0.810
Diameter of propeller	D_P (m)	9.860
Rudder area	A_R (m^2)	112.5
Rudder height	H_R (m)	15.80
Waterplane area	A_w (m^2)	16750
Radius of gyration	k_{zz} (m)	80
Propeller Longitudinal Position	x_P (m)	–154.33
Rudder Longitudinal Position	x_R (m)	–160.00
Frontal projected area	A_F (m^2)	1056
Lateral projected area	A_L(m^2)	4524.2

Table 3 Quantitative validation of the KVLCC2 turning maneuver simulation in deep water at 15.5 kn

Variables	Experiment (FRMT)	Simulation	Absolute error	Relative error
AD/L_{pp}	3.08	3.25	0.17	5.5 %
TR/L_{pp}	1.25	1.31	0.06	4.8 %
TD/L_{pp}	3.08	3.01	0.07	2.3 %
r	–0.428	–0.422	0.006	1.4 %
U/U_0	0.36	0.298	0.062	17.2 %
β (deg)	20.2	21.07	0.87	4.3 %

3.2 Validation for shallow water

Figure 7 shows the turning maneuver in shallow water. The comparison is with three measurement experiments. The turning circle diameter of the 35° port side increased due to the shallow water effect. The variance among the three experimental conditions is normal due to typical increases in uncertainty in shallow water, and each experiment has a distinct setup. The shallow-water validation is performed for the extreme condition at h/T=1.2, where the influence of shallow-water depth becomes significant. Table 4 presents the numerical results, which are compared with the FRMT-15 experimental data, while the FRMT-99 and EMP results are included as additional references to evaluate prediction consistency. Larger deviations are observed in the speed change and drift angle, with relative errors of 16 % and 32.6 %, respectively. These deviations are mainly attributed to stronger shallow-water effects, including increased hydrodynamic interactions, blockage effects, and uncertainty associated with empirical shallow-water correction formulations. Nevertheless, the predicted values remain close to the EMP results, with smaller differences in speed change and drift angle at 10.5 % and 3 %, respectively. This indicates that the established model captures the main physical trends of shallow water maneuvering behavior. To further validate the drift angle and speed change in shallow water, numerical results reported by Li et al. [13] for KVLCC2 under shallow water conditions are compared with the present study. At h/T=1.2, they predicted

the speed change during steady turning and the drift angle with corresponding values of 0.6650 and 2.73°, respectively, indicating the established modular model's ability to replicate extreme shallow water conditions. The Raven shallow-water resistance correction is applied beyond its formal ITTC applicability range ($h/T \geq 2.5$) for the h/T=1.2 case. Therefore, the shallow-water validation results at this depth are interpreted as model predictions rather than fully validated quantitative results. The agreement with experimental data confirms the qualitative trends, but independent experimental or CFD validation at these extreme shallow-water conditions remains desirable.

Table 4 Quantitative validation of the KVLCC2 turning maneuver simulation in shallow water against FRMT and EMP results at 7 kn

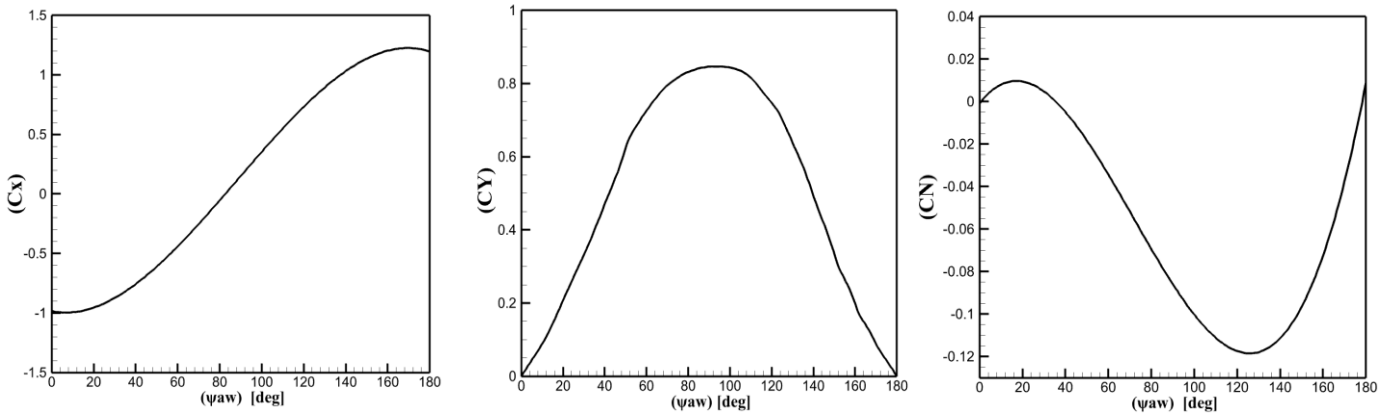
Variables	Experiment FRMT-15		FRMT-99 EMP-15	Simulation	Absolute error	Relative error
AD/L_{pp}	2.92	—	5.04	3.21	0.297	9.9 %
TR/L_{pp}	2.08	—	4.18	2.174	0.094	4.5 %
TD/L_{pp}	—	—	8.52	4.347	—	—
r'	–0.45	–0.44	–0.25	–0.459	0.009	2 %
U/U_0	0.81	0.86	0.76	0.68	0.13	(16 % FRMT-15), (10.5 % EMP-15)
β (°)	1.9	4.4	2.6	2.52	0.62	(32.6 % FRMT-15), (3 % EMP-15)

3.3 Comparison of turning maneuver at various *h/T* ratios

As shown in Figure 8, the diameter of the turning circle decreases as the h/T ratio increases, and hydrodynamic interaction with the bottom is reduced, allowing the ship to turn easily. In shallow water, the added mass coefficients increase due to water inertia and bottom effects. In addition, the hydrodynamic damping coefficients are higher in shallow water and decrease as h/T increases.

As seabed interaction decreases and the vessel turns smoothly, the yaw rate increases with increasing h/T ratio. Additionally, as water depth increases, the lateral force causes the ship to swing more quickly, increasing the drift angle. The speed change U/U_0 increases as the h/T ratio is decreased.

In this study, three water depth-to-draft ratios (h/T) are selected (1.2, 1.5, and 3). Five wind type conditions are analyzed, including headwind, oblique headwind, beam wind, aft quartering wind, and following wind. Simulations are conducted at wind speeds of 5, 10, 15, and 20 m/s, for both full ship speed (design speed) and 75 % of full ship speed. Table 5 summarizes the simulation scenarios, corresponding to the schematic view shown in Figure 3. The results presented for h/T=1.2 and 1.5 are based on the extrapolated shallow-water correction; therefore, they are interpreted as model predictions. The trends are physically consistent, and the validation at h/T=1.2 shows reasonable agreement with experimental data.



a) longitudinal coefficients b) lateral coefficients c) yaw moment coefficients

Fig. 4 The aerodynamic coefficients related to the KVLCC2 model

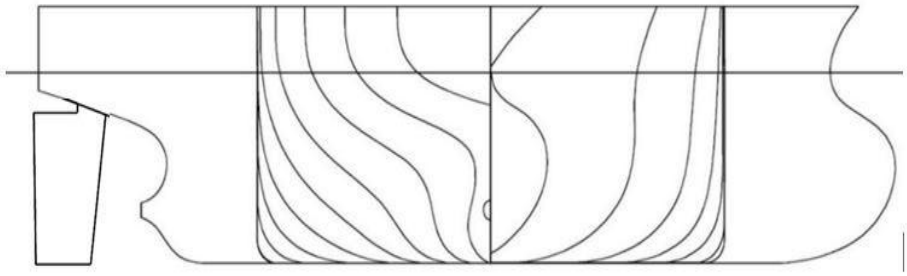


Fig. 5 Hull plan and profile of the KVLCC2 model

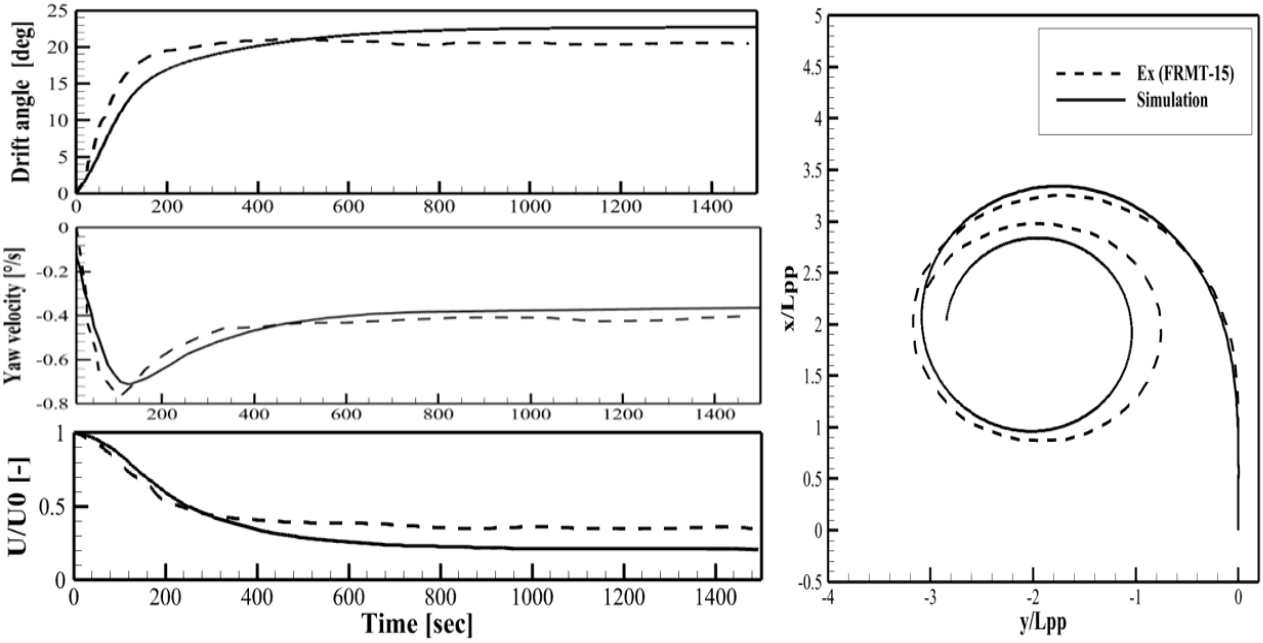


Fig. 6 Deep-water validation, including turning trajectory and related indices at full ship speed 15.5 kn (7.973 m/s)

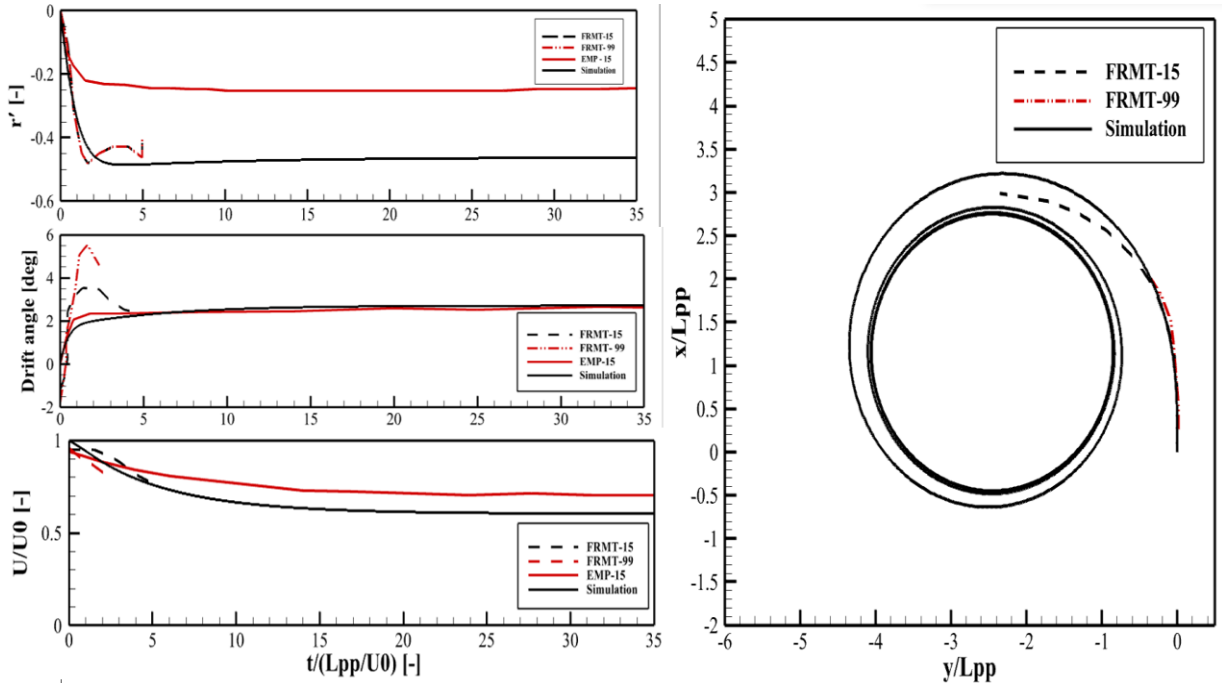


Fig. 7 Shallow-water validation, including turning trajectory at 35° port side and related indices at 7 kn (3.60 m/s)

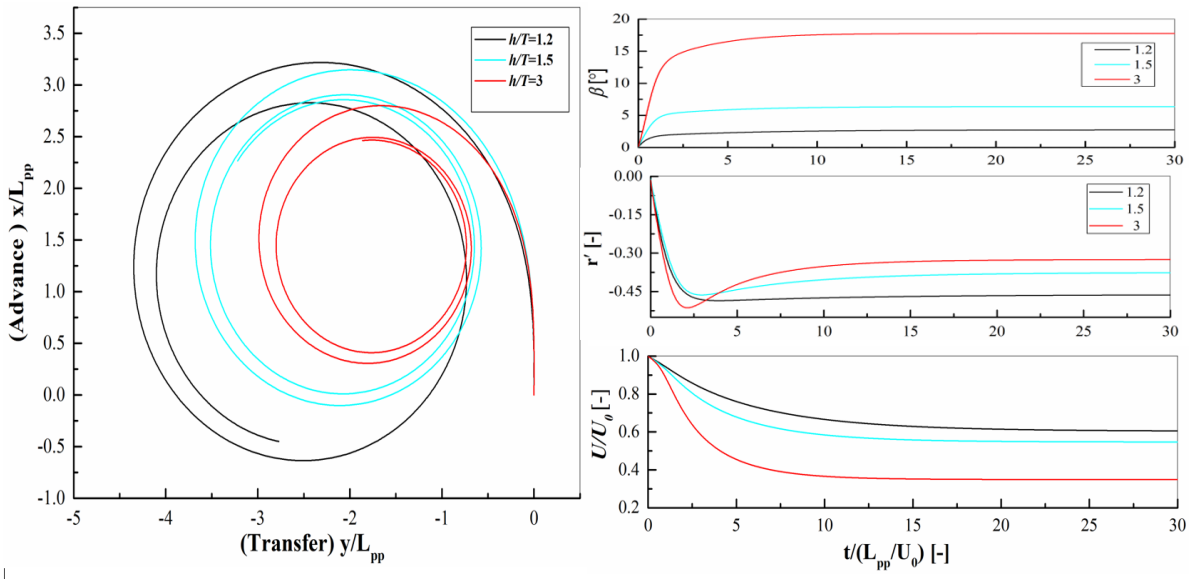


Fig. 8 Comparison of the turning circle trajectory at different *h/T* ratios at 15.5 kn (7.973 m/s)

Table 5 Simulation scenarios

Scenarios	Ship speed (m/s)	True wind angle (bow to wind) (°)	*h/T*	Wind speed (m/s)
1	Full at (7.973 m/s) 15.5 knots and 75 % of full speed at (5.980 m/s) 11.625 knots	No wind	1.2, 1.5, 3	0
2		Headwind (0 °)		5, 10, 15, 20
3		Oblique headwind (15°, 30°, 45°, 60°, 75°)		
4		Beam wind (90 °)		
5		Aft quartering wind (105°, 120°, 135°, 150°, 165°)		
6		Following wind (180°)		

4. Simulation and analysis of results

Table 6 presents the numerical values of the turning maneuver indices at various *h/T* ratios and ship speeds, without wind effect, to clearly illustrate changes across operational conditions. The maneuvering indices are estimated using the following equations:

$$
\begin{aligned}
AD/L &= \frac{|x(t_{90}) - x_0|}{L} \\
TR/L &= \frac{|y(t_{90}) - y_0|}{L} \\
TD/L &= \frac{|y(t_{180}) - y_0|}{L} \\
\beta &= \tan^{-1}(-v/u) \\
r &= \frac{\partial \psi}{\partial t} \\
L_D &= \max(Y(t)) \\
U/U_0 &= \sqrt{u^2 + v^2}/U_0
\end{aligned}
\tag{23}
$$

Table 6 Maneuvering indices values without wind influence at various water depths

Ship speed	Full speed (7.973 m/s) 15.5 kn			75 % of full speed (5.980 m/s) 11.625 kn		
h/T	1.2	1.5	3	1.2	1.5	3
AD/L_{pp}	3.217	3.147	2.77	3.204	3.14	2.767
TR/L_{pp}	–2.174	–1.84	–1.493	–2.1605	–1.834	–1.49
r'	–0.458	–0.389	–0.353	–0.463	–0.392	–0.354
U/U_0	0.6759	0.609	0.414	0.6758	0.610	0.415
β (°)	2.516	6.056	16.85	2.519	6.07	16.87

In this section, the shallow-water correction employed in this study is applied beyond its formal ITTC applicability range for the h/T=1.2 and 1.5 cases. Consequently, the results presented for these two depth ratios are model predictions based on the extrapolated correction, rather than fully validated quantitative results. The h/T=3.0 case lies within the formal applicability range of the adopted shallow-water resistance correction. In addition, predicted wind-induced changes of the order of 1-4 % are treated as small or marginal trends within the present model rather than as quantitatively significant effects, particularly when these changes are comparable to or smaller than the corresponding response-specific validation discrepancies.

4.1 Headwind scenarios

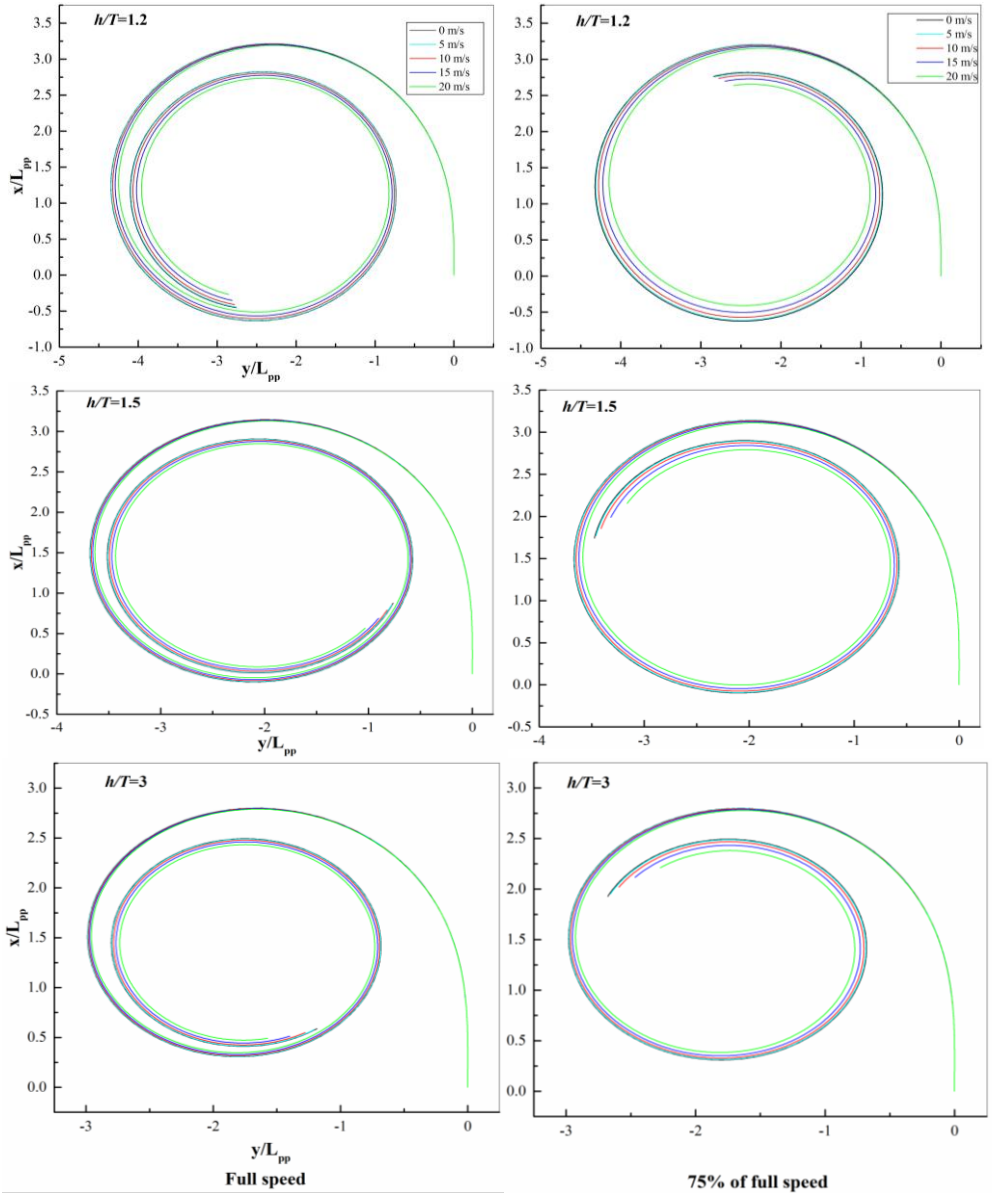
In the case of a headwind, at full ship speed and wind speeds exceeding 10 m/s, the diameter of the turning circle is slightly reduced. This occurs because the headwind helps maintain the ship along its turning path, allowing the ship to turn tightly, as shown in Figure 9(a). When the ship speed is reduced to 75 % of full speed, wind speeds exceeding 5 m/s become influential. However, the reduction becomes noticeable in terms of maximum advance and transfer at h/T=1.2. This reduction effect diminishes as the h/T ratio increases.

As the headwind counteracts the natural yawing oscillation of the ship, the variation in heading is reduced, resulting in a decrease in yaw-rate magnitude |r|, as illustrated in Figure 9(b). As the water depth increases, the reduction of yaw rate magnitude decreases, with the largest reduction observed under shallow water conditions at h/T=3. As the h/T ratio decreases, the reduction in yaw rate becomes less pronounced.

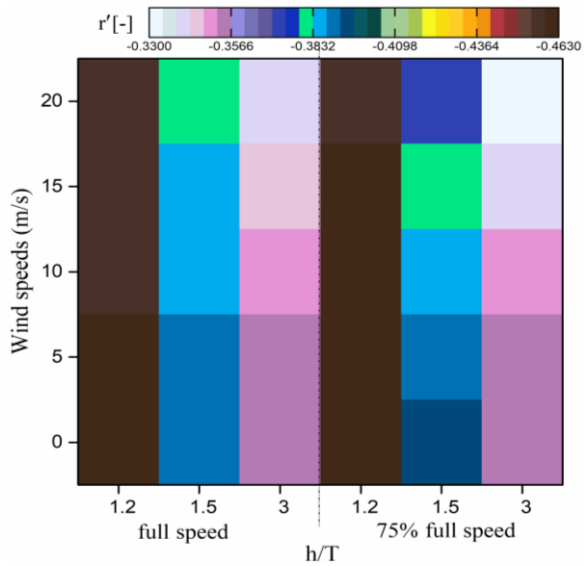
In Figure 9(c), the headwind increases the lateral drift tendency, increasing the drift angle magnitude. The drift angle increases by 1.2 %, 2.8 %, and 5.2 % at h/T=3, with corresponding values of 17.05°, 17.32°, and 17.7° at wind speeds greater than 5 m/s at full ship speed; reaching to 2.1 %, 5.2 %, and 10.2 % with corresponding values of 17.2°, 17.7°, and 18.6°, respectively, when the ship speed reduced to 75 %. These percentages decrease as the h/T ratio increases. Further reducing ship speed increases the drift angle across all h/T ratios.

Figure 9(d) shows that increasing headwind speed reduces forward speed, with the effect becoming pronounced at wind speeds above 5 m/s. Under full speed conditions, the largest reduction is observed at h/T=3, with reductions of approximately 2.1 %, 4.7 %, and 8.5 % as wind speed increases, corresponding to values of 0.406, 0.395, and 0.379, respectively. At 75 % of full speed, the reduction becomes more pronounced across all h/T ratios. These results indicate that reduced ship speed increases sensitivity to wind-induced resistance, while water depth effects modify the hydrodynamic response. The combined influence of aerodynamic forces and depth-dependent hydrodynamic effects therefore governs the variation in forward speed.

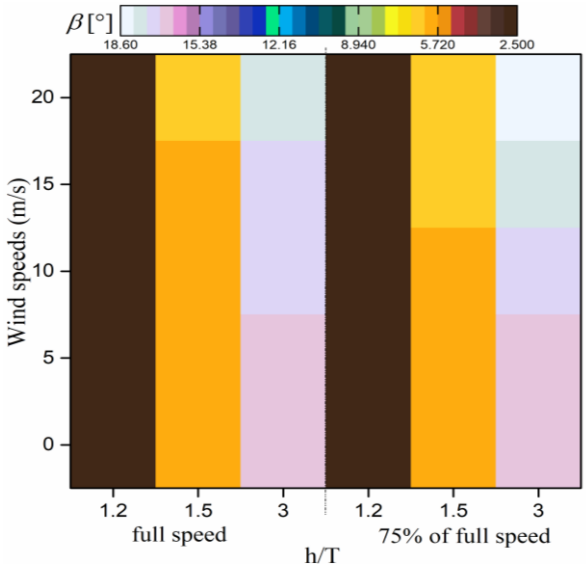
Accordingly, wind-induced changes of only a few percent (approximately 1-4 %) are interpreted as small or marginal predicted trends within the present model.



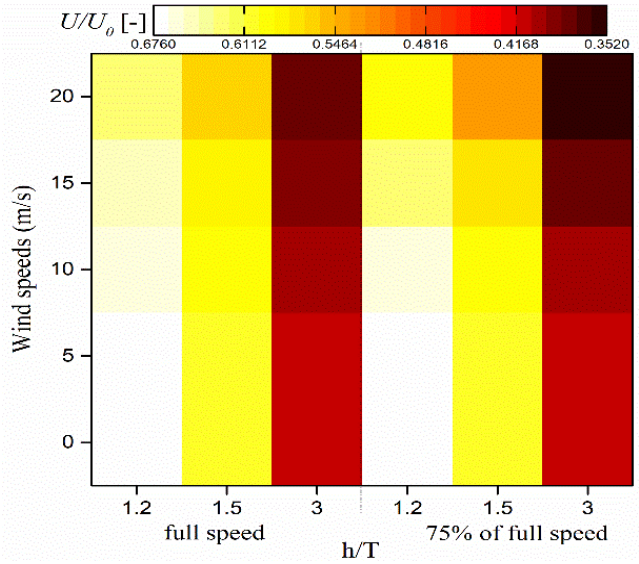
a) Turning trajectory at full and 75 % of full ship speed



b)Yaw rate at full and 75 % of full ship speed



c) Drift angle at full and 75 % of full ship speed



d) Forward speed changes at full and 75 % of full ship speed

Fig. 9 Comparison of turning trajectory and indices at different *h/T* ratios at full and 75 % of full ship speed for the headwind scenarios (0°)

4.2 Oblique headwind scenarios

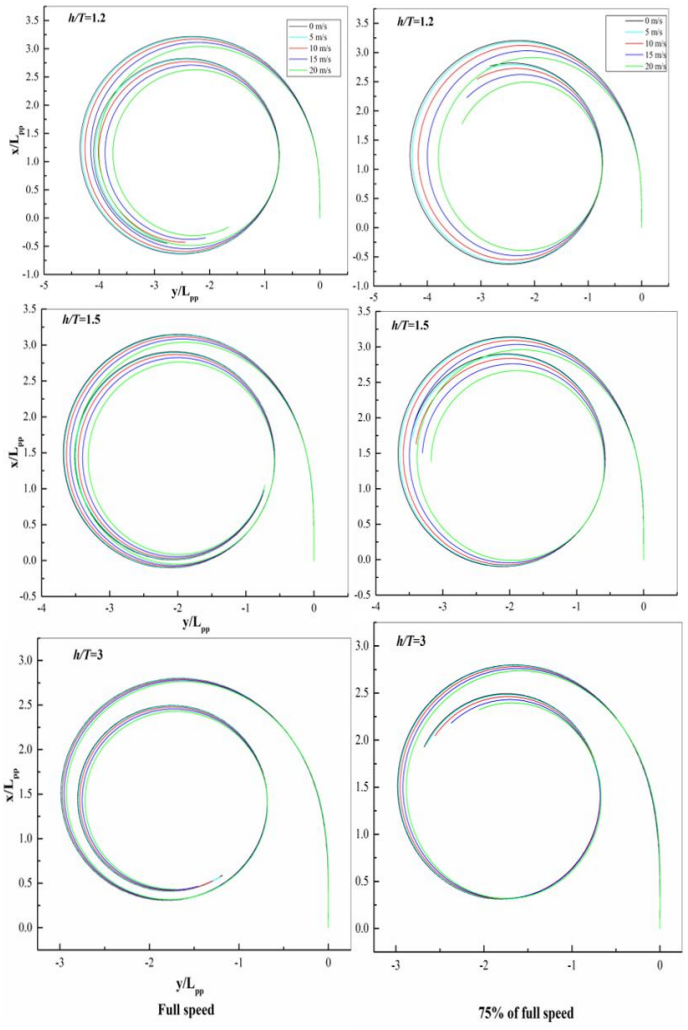
When the wind acts in the same direction as the ship's turning motion, as shown in Figure 10(a), the reduction in maximum advance and transfer increases with increasing wind obliqueness from 15° to 75° and with increasing wind speed, even at *h/T*=3. This effect is more pronounced in shallow water (*h/T*=1.2) and decreases as the *h/T* ratio increases. At *h/T*=1.2, the maximum advance decreases by 1.5 %, 3.2 %, and 5.5 % with values of 3.169, 3.114, and 3.039, while the transfer decreases by 2.0 %, 4.5 %, and 7.5 % with values of 2.1285, 2.0765, and 2.0095 at wind speeds of 10, 15, and 20 m/s, respectively. When the ship speed is reduced to 75 % of full speed, these reductions become more noticeable, reaching 2.6, 5.5, and 9 % for advance, with corresponding values of 3.121, 3.028, and 2.913, and 3.5 %, 7.5 %, and 12.5 % for transfer, with values of 2.084, 1.9985, and 1.896 under the same wind conditions. Conversely, when the wind acts opposite to the ship's turning direction, as shown in Figure 10(a*), the turning trajectory is markedly affected, with increases in both advance and transfer, particularly at *h/T*=1.2. This effect decreases as the *h/T* ratio increases. The increase becomes more pronounced with increasing wind obliqueness and wind speed. At *h/T*=1.2 and 75 % of full speed, the changes in advance and transfer are relatively limited at lower wind speeds (5 and 10 m/s) but become pronounced under higher wind speeds and larger oblique wind angles. At a wind angle of 75°, 75 % of full speed and wind speeds of 10, 15, and 20 m/s, the advance increases by 4.7 %, 12 %, and 25.5 %, with corresponding values of 3.356, 3.587, and 4.023, while the transfer increases by 6.0 %, 15 %, and 34 % with values of 2.289, 2.492, and 2.9005, respectively. These results indicate that increasing wind obliqueness and wind speed, combined with reduced ship speed, intensify the adverse effect of wind on turning performance, with a noticeable influence even at *h/T*=3 for wind speeds above 5 m/s. The smaller changes of approximately 1-4 % are interpreted as marginal predicted trends within the trajectory, considering the corresponding validation discrepancies, rather than as quantitatively significant changes.

When the wind acts in the same direction as the ship's turning motion, the yaw-rate magnitude |r| increases with increasing wind speed, with a more pronounced effect at *h/T*=1.2 than at *h/T*=1.5. This indicates that the wind-induced yaw moment amplifies the natural turning response under shallow-water conditions. At *h/T*=3, however, the yaw-rate magnitude decreases slightly, indicating that the wind partially counteracts the turning response in deeper water. As shown in Figure 10(b), at *h/T* = 1.2, |r| increases to 0.47, 0.48, and 0.49 at wind speeds of 10, 15, and 20 m/s, corresponding to increases of 1.7 %, 3.6 %, and 6 %; the changes of 1.7 % and 3.6 % are interpreted as marginal trends within the present model, while the 6 % change at 20 m/s is described as a more pronounced predicted trend. In contrast, at *h/T*=3, |r| decreases to 0.35, 0.34, and 0.335, corresponding to decreases of 1.2 %, 2.8 %, and 5.1 % under the same wind conditions. The influence of wind becomes more significant when ship speed is reduced to 75 % of full speed. At *h/T*=1.2, |r| increases to 0.48, 0.49, and 0.51, corresponding to increases of 3.0 %, 5.9 %, and

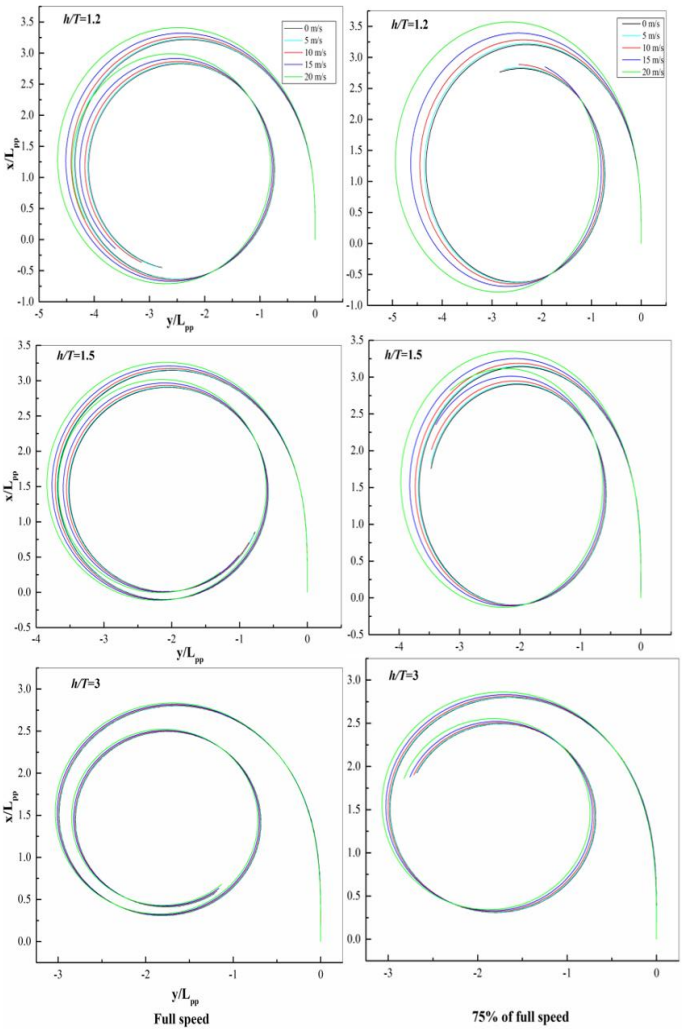
9.6 % for wind speeds above 5 m/s. At h/T=3, |r| decreases to 0.35, 0.34, and 0.32, corresponding to decreases of 2.2 %, 5 %, and 9.3 % under the same conditions. The increase in |r| at h/T=1.2 and 1.5 becomes more pronounced as wind obliqueness increases up to 75°, whereas at h/T=3, |r| decreases with increasing obliqueness. When the wind acts opposite to the turning direction, as shown in Figure 10(b*), the yaw-rate magnitude decreases at h/T=1.2 and 1.5 because the wind-induced yaw moment opposes the natural turning moment. At h/T=1.2, |r| decreases to 0.45, 0.44, and 0.42, corresponding to decreases of 2 %, 4.3 %, and 8 % for wind speeds above 5 m/s; these reductions increase to 3.4 %, 7.9 %, and 14.9 % with values of 0.45, 0.43, and 0.39 when ship speed is reduced to 75 %. At h/T=3, the yaw-rate magnitude slightly increases rather than decreases, indicating that the opposing wind has a weaker influence on the yaw response in deeper water. These changes become more pronounced as wind obliqueness increases up to 75°.

The drift angle magnitude increases with both wind obliqueness and wind speed when the wind acts in the same direction as the ship's turning, with a more pronounced effect observed at h/T=3. As shown in Figure 10(c), this increase becomes less pronounced as the h/T ratio decreases. At h/T=3, the drift angle increases by 5.6 %, 13.3 %, and 25.3 %, with values of 17.8°, 19.1°, and 21.1° for wind speeds of 10, 15, and 20 m/s, respectively. These values increase further to 10 %, 25 %, and 49.7 % when the ship speed is reduced to 75 %. This behavior is attributed to reduced hydrodynamic resistance to lateral moment, leading to an increase in the drift angle. These results indicate a more pronounced predicted drift response as wind obliqueness and wind speed increase. When the wind acts in the opposite direction, the drift angle magnitude decreases; this reduction occurs because the wind-induced yaw moment counteracts the natural turning motion, reducing the lateral deviation during maneuver, with reductions of 4.8 %, 9.7 %, and 17.1 % with values of 16.1°, 15.2°, and 13.97° for wind speeds of 10, 15, and 20 m/s, respectively. These reductions increase to 7.6 %, 17 %, and 29.5 % with values of 15.6°, 14°, and 11.9° as the ship speed decreases, as shown in Figure 10(c*), because the lower forward speed decreases the hydrodynamic resistance against wind-induced lateral motion, allowing the wind-induced yaw moment to have a stronger influence on the ship’s trajectory.

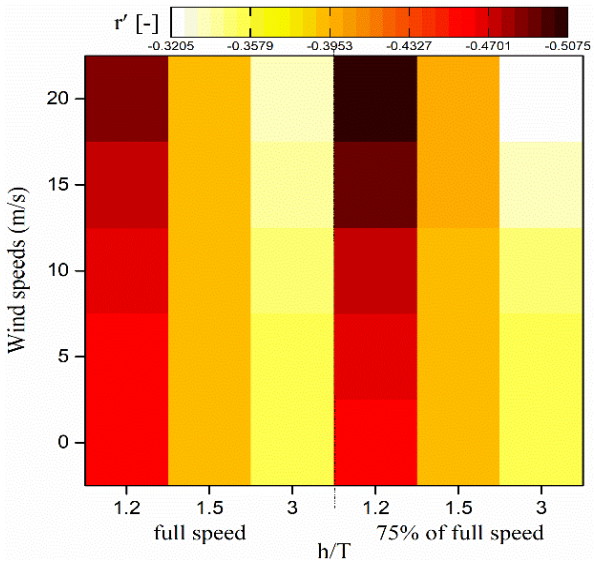
In Figure 10(d), the reduction in forward speed change becomes more pronounced at h/T=3, where the wind-induced aerodynamic force has a larger relative influence on the longitudinal force balance because the shallow water-induced increase in hydrodynamic resistance is smaller. This effect decreases as the h/T ratio decreases, indicating weaker sensitivity of forward speed to wind forces under shallow water conditions. When the ship speed is reduced to 75 % of full speed, the relative influence of the aerodynamic forces increases further, resulting in a more pronounced change in speed. Conversely, when the wind acts opposite to the ship's turning direction, as shown in Figure 10(d*), the forward speed change has a relatively small decrease at h/T=1.2, while it becomes more pronounced as the h/T ratio increases. The largest increase occurs at h/T=3, where reduced hydrodynamic resistance allows wind-induced forces to have a greater relative influence on the longitudinal force balance. This tendency becomes more pronounced as the ship speed decreases. In addition, increasing wind speed and obliqueness increase aerodynamic forces and consequently amplify the change in speed response.



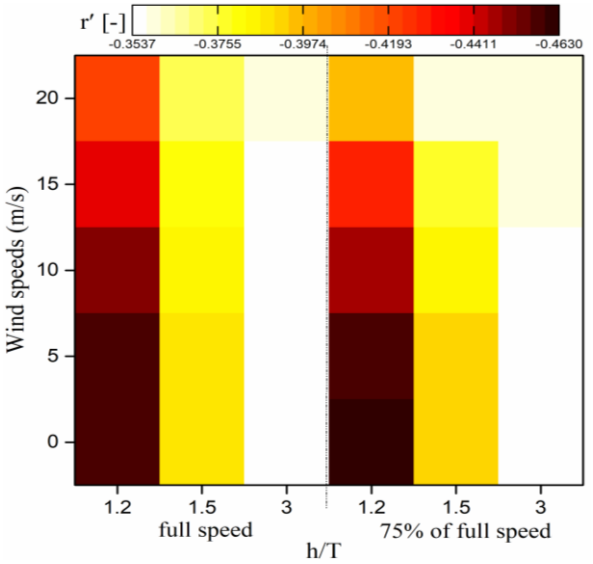
a) Turning trajectory when the wind acts in the same direction



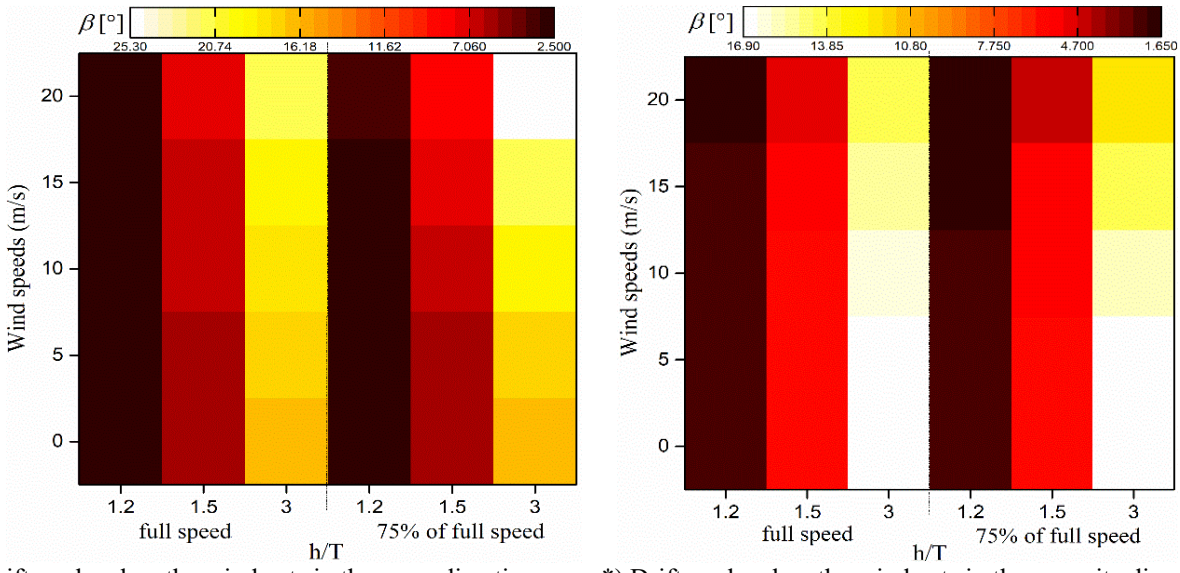
a*) Turning trajectory when the wind acts in the opposite direction



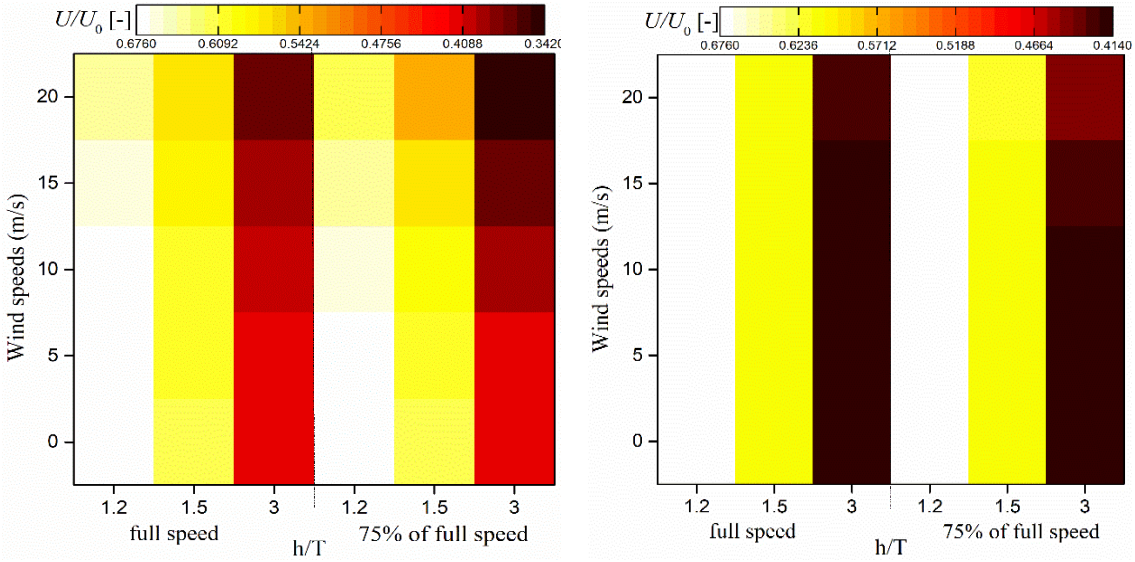
b) Yaw rate when the wind acts in the same direction



b*) Yaw rate when the wind acts in the opposite direction



c) Drift angle when the wind acts in the same direction c*) Drift angle when the wind acts in the opposite direction



d)Speed changes when the wind acts in the same direction d*) Speed changes when the wind acts in the opposite direction

Fig. 10 Comparison of turning trajectory and indices at different *h/T* ratios at full and 75 % of full ship speed for the oblique headwind scenarios at (45°)

4.3 Beam wind scenarios (90°)

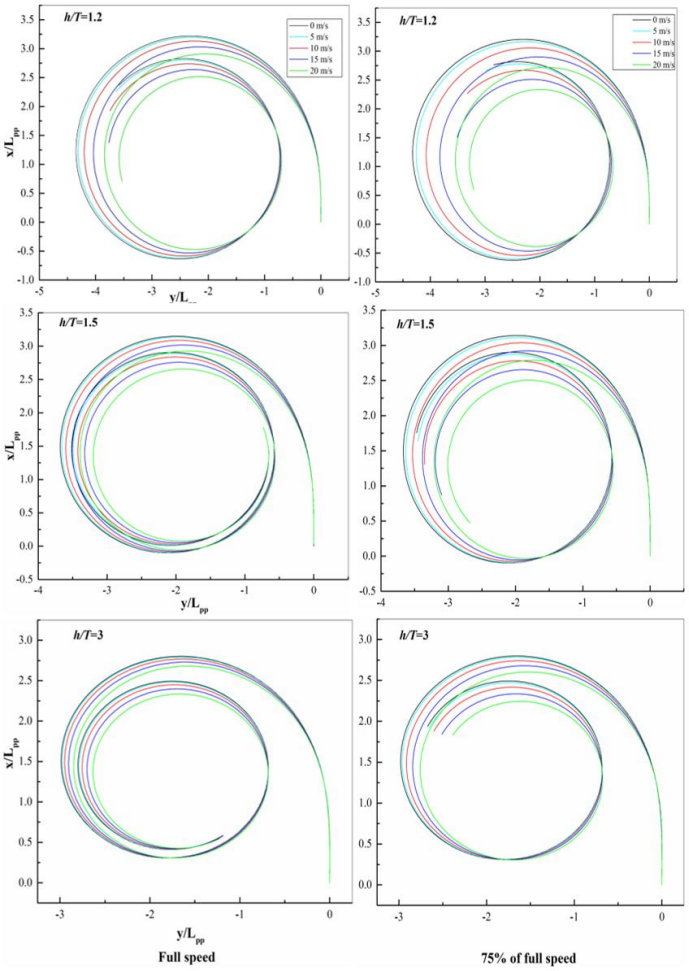
When the wind acts perpendicular to the turning path in the same direction as the ship is turning, as shown in Figure 11(a), advance and transfer decrease noticeably at *h/T*=1.2. The advance decreases by 2.8 %, 5.8 %, and 9.6 %, with corresponding values of 3.129, 3.031, and 2.907, while the transfer decreases by 3.5 %, 7.1 %, and 11.7 %, with corresponding values of 2.1, 2.019, and 1.92 for wind speeds of 10, 15, and 20 m/s, respectively. These reductions further increase to 4.6 %, 9.6 %, and 15 % with corresponding values of 3.056, 2.898, and 2.72 in advance, and to 5.6 %, 11.5 %, and 18 %, with values of 2.0375, 1.9115, and 1.7695 in transfer, as the ship speed is reduced to 75 % of full speed. Even at *h/T*=1.5 and 3, the reduction trend remains evident. In contrast, when the wind acts in the opposite direction, as displayed in Figure 11(a*), both advance and transfer increase significantly at *h/T*=1.2. The advance increases by 3.4 %, 7.3 %, and 14.3 % with corresponding values of 3.315, 3.451, and 3.676, while the transfer increases by 4 %, 9.1 %, and 18.3 % with corresponding values of 2.2555, 2.372, and 2.571, respectively, at the same wind speeds. When ship speed is reduced, these increases intensify to 5.5 %, 14.1 %, and 31 % with values of 3.381, 3.656, and 4.202 for advance and 7 %, 18 %, and 41.8 % with values of 2.31, 2.5495, and 3.063 for transfer, respectively. It is worth noting that at a wind speed of 10 m/s and when the wind acts in both directions, the increase in advance and transfer is interpreted as marginal at full ship speed. However, when

the ship speed is reduced, the wind effect becomes noticeable at all *h/T* ratios, with the highest impact at *h/T*=1.2 and diminishing as the *h/T* ratio increases.

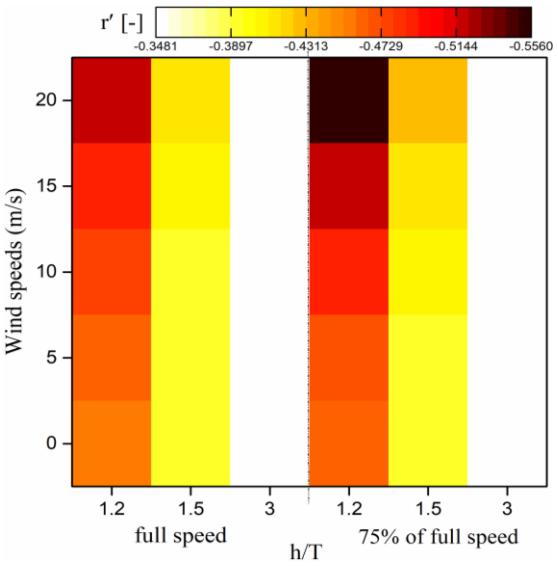
In Figure 11(b), the yaw-rate magnitude |r| increases at *h/T*=1.2 and 1.5 when the wind acts perpendicularly in the same turning direction. At *h/T*=1.2, |r| increases to 0.47, 0.49, and 0.52 at wind speeds of 10, 15, and 20 m/s, corresponding to increases of 3.4 %, 7.4 %, and 12.5 %, respectively. The 3.4 % change reflects a marginal predicted trend in the current model, whereas the 7.4 % and 12.5 % changes represent more pronounced predicted trends. These increases become larger when the ship speed is reduced to 75 %: |r| rises to 0.49, 0.52, and 0.56, corresponding to increases of 5.8 %, 12.3 %, and 20 %. This indicates that the beam wind amplifies the yaw response under shallow-water conditions. However, at *h/T*=3, the yaw-rate magnitude decreases slightly, indicating that the wind-induced yaw moment partially counteracts the turning response in deeper water. When the wind acts opposite to the turning direction, as shown in Figure 11(b*), the yaw-rate magnitude decreases at all *h/T* ratios due to the opposing wind-induced yaw moment. At *h/T*=1.2, |r| decreases to 0.44, 0.42, and 0.39, corresponding to decreases of 3.6 %, 8.4 %, and 15.8 %, respectively, at wind speeds above 5 m/s at full speed. The 3.6 % change reflects a marginal predicted trend in the current model, whereas the larger reductions at higher wind speeds indicate a noticeable predicted response. These reductions become larger when ship speed is reduced to 75 %: |r| decreases to 0.43, 0.39, and 0.32, corresponding to decreases of 6.5 %, 15.6 %, and 30.8 %.

In Figure 11(c), the drift angle magnitude reaches its highest values at all *h/T* ratios when the wind acts perpendicular to the ship's turning direction, with an evident increase at *h/T*=3. This behavior is attributed to the strong lateral aerodynamic force generated by the beam wind and the reduced hydrodynamic restoring capability against wind-induced lateral motion as the *h/T* ratio increases. At *h/T*=3, the angle increases by 6.8 %, 15.9 %, and 29.5 % with corresponding values of 18°, 19.5°, and 21.8° for wind speeds of 10, 15, and 20 m/s, respectively; these values further increase to 12.3 %, 29.2 %, and 55.6 % with corresponding values of 18.9°, 21.8°, and 26.3° when the ship speed is reduced to 75 %, due to the reduced hydrodynamic resistance against lateral motion. When the wind acts in the opposite direction, as shown in Figure 11(c*), the drift angle decreases at all *h/T* ratios. This reduction is significant at *h/T*=3 and diminishes as *h/T* decreases. At *h/T*=3, the drift angle decreases by 6.5 %, 14.2 %, and 24.1 % with corresponding values 15.8°, 14.5°, and 12.8° for wind speeds of 10, 15, and 20 m/s, respectively; these values further decrease to 11.2 %, 23.9 %, and 39.7 % with corresponding values of 14.9°, 12.8°, and 10.2° as the speed of the ship is reduced, indicating that lower ship speed enhances the influence of the wind-induced lateral force on drift behavior.

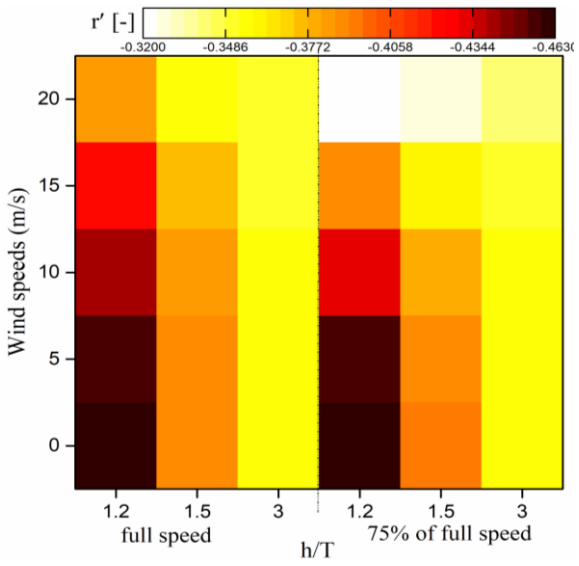
The forward speed change response under perpendicular wind conditions is strongly influenced by wind direction, *h/T* ratio, and ship speed, as shown in Figure 11(d) and Figure 11(d*). Forward speed change decreases when the wind acts in the same direction, particularly at *h/T*=3; this reduction becomes less pronounced as *h/T* decreases, as shown in Figure 11(d). This behavior may be attributed to wind-induced lateral force and yaw moment, which modify sway and yaw motion, drift angle, and turning trajectory and consequently increase hydrodynamic resistance. At *h/T*=3, the speed change decreases by 2.8 %, 6.2 %, and 10.5 % with corresponding values of 0.403, 0.389, and 0.371, respectively, for wind speeds above 5 m/s; these values further decrease to 4.9 %, 10.5 %, and 17.3 % with corresponding values of 0.39, 0.37, and 0.34 as the ship speed is reduced. In the opposite direction, as shown in Figure 11(d*), the change in forward speed increases, with a more pronounced predicted effect at *h/T*=3; this response is associated with the modified turning behavior caused by the opposing wind-induced lateral force and yaw moment, which alter the sway/yaw dynamics and the resulting hydrodynamic resistance balance, producing a smaller speed loss during the turn. This increase becomes less pronounced as the *h/T* ratio decreases. The forward speed increases by 3 %, 6.7 %, and 12.3 % with corresponding values of 0.42, 0.44, and 0.47 at wind speeds exceeding 5 m/s; these ratios increase to 5.3 %, 12.2 %, and 23 % with corresponding values of 0.44, 0.47, and 0.51 as the ship speed is reduced to 75 %. The smaller predicted changes of the order 1-4 % in forward speed are interpreted as a marginal predicted response.



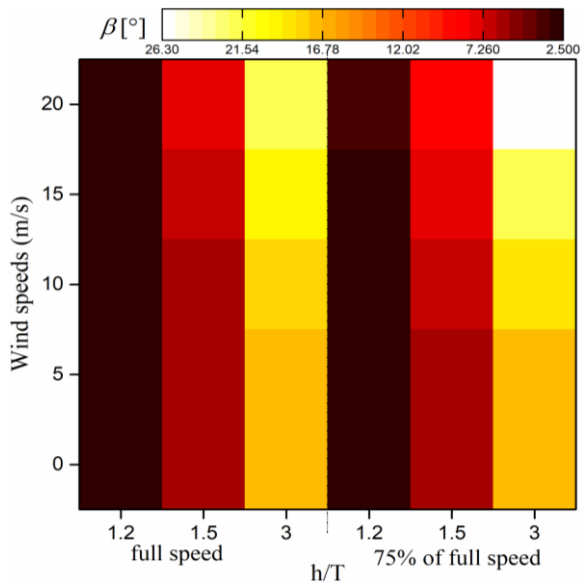
a) Turning trajectory when the wind acts in the same direction .a*) Turning trajectory when the wind acts in the opposite direction



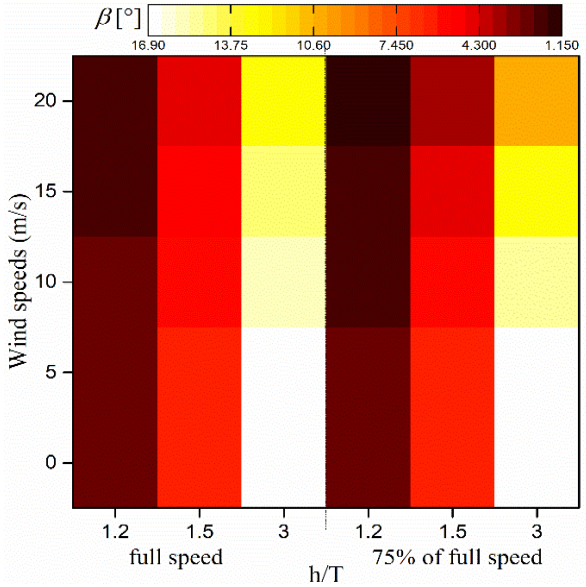
b) Yaw rate when the wind acts in the same direction



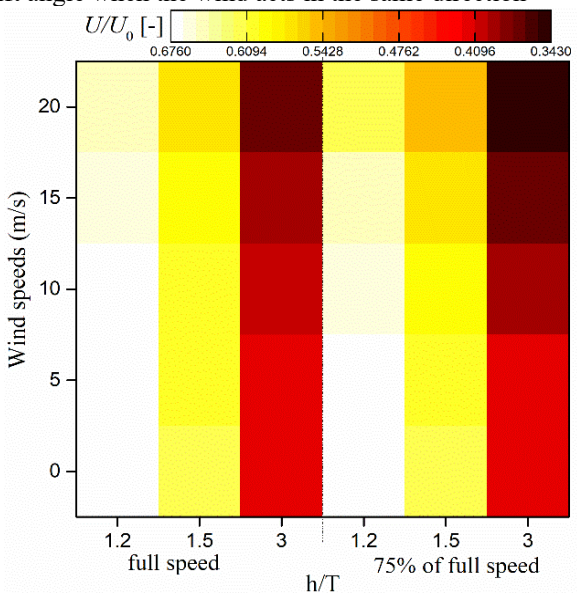
b*) Yaw rate when the wind acts in the opposite direction



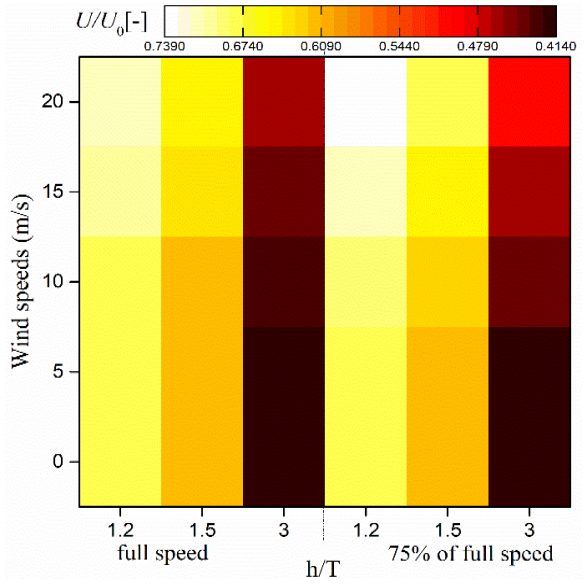
c) Drift angle when the wind acts in the same direction



c*) Drift angle when the wind acts in the opposite direction



d) Speed changes when the wind acts in the same direction



d*) Speed changes when the wind acts in the opposite direction

Fig. 11 Comparison of turning trajectory and indices at different *h/T* ratios at full and 75 % of full ship speed for the beam wind scenarios (90°)

4.4 Aft quartering wind scenarios

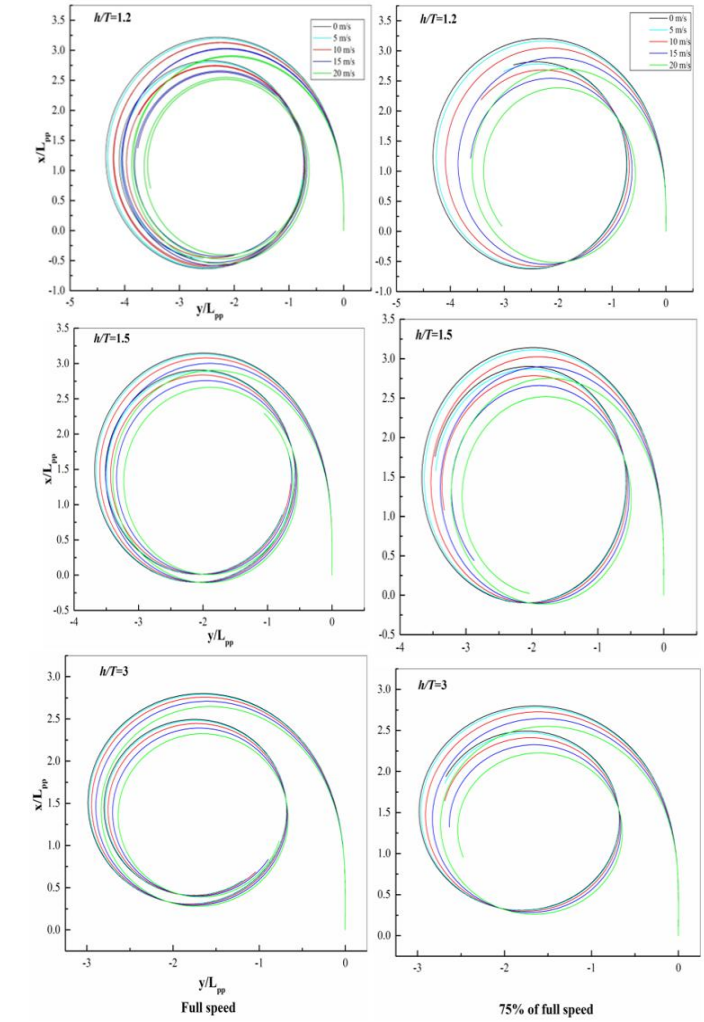
When the wind acts in the same or opposite direction to the ship's turning motion, the turning trajectory exhibits the maximum reduction or increase in advance and transfer, respectively, at a wind angle of approximately 120°. This effect is most noticeable at *h/T*=1.2 and gradually decreases as the *h/T* ratio increases. At this wind angle, when the wind acts opposite to the ship's turning direction, the advance increases by 3.9 %, 9.4 %, and 18.8 %, with corresponding values of 3.342, 3.519, and 3.822, while the transfer increases by 4.9 %, 12.2 %, and 24.9 %, with values of 2.281, 2.438, and 2.7155, for wind speeds above 5 m/s. The 3.9 % change in advance is interpreted as a small, predicted trend within the present model, whereas the larger changes at higher wind speeds indicate a noticeable response. These increases become more pronounced when the ship speed is reduced to 75 % of full speed, reaching 7.1 %, 18.5 %, and 43.3 % for advance, with values of 3.431, 3.797, and 4.590, respectively; and 9.2 %, 24.6 %, and 60.0 % for transfer, with values of 2.3585, 2.6915, and 3.462, respectively. A noticeable influence on the turning trajectory is also observed at *h/T*=1.5 and *h/T*=3 for wind speeds above 5 m/s, although the effect is less pronounced. The highest impact at a wind angle of 120° is attributed to the large aerodynamic yaw moment generated by the wind force acting with a relatively large lever arm, resulting in significant changes in both

advance and transfer. Beyond this angle, at approximately 135°, as shown in Figure 12(a) and (a*), the trajectory variation gradually decreases as the wind shifts further toward aft-quartering wind angles.

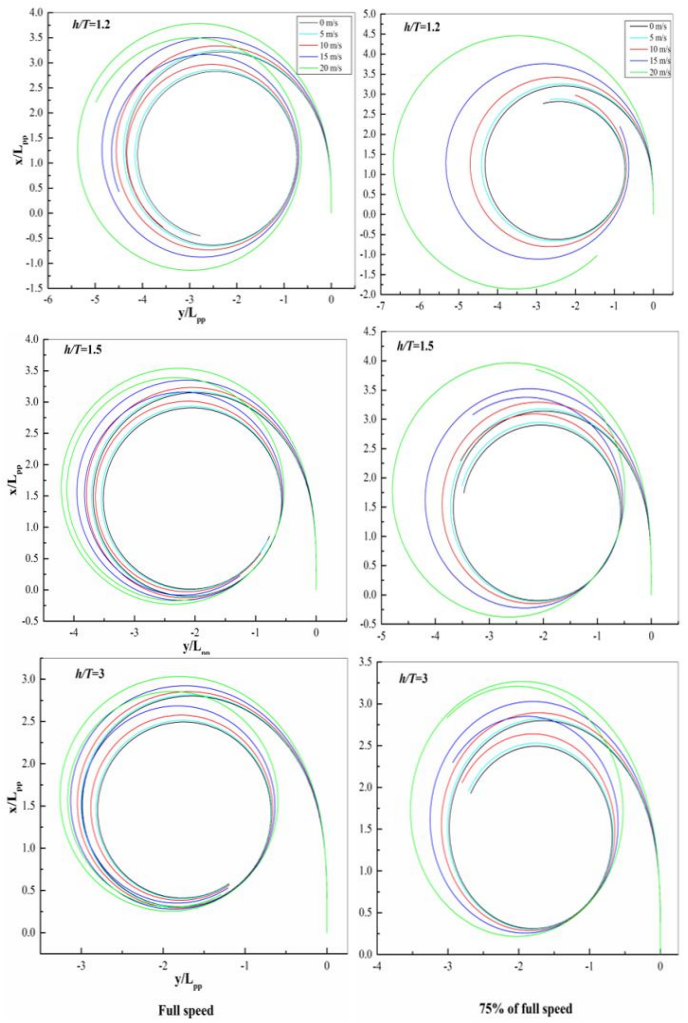
At approximately 120°, the yaw-rate magnitude |r| exhibits its largest increase at h/T=1.2 when the wind acts in the same direction as the ship's turning. This behavior is attributed to the stronger shallow-water influence on hydrodynamic maneuvering characteristics, which modifies yaw damping and restoring forces and increases the sensitivity of the yaw response to wind-induced moments. At h/T=1.2, |r| increases to 0.49, 0.51, and 0.53 at wind speeds above 5 m/s, corresponding to increases of 4.3 %, 9.3 %, and 15.7 % relative to the no-wind baseline. These increases become more pronounced when the ship speed is reduced to 75 % of full speed, reaching 7.3 %, 15.5 %, and 25.6 % with values of 0.51, 0.53, and 0.58. At h/T=1.5 and 3, the maximum response occurs at larger wind angles due to the changing balance between the wind-induced yaw moment and hydrodynamic restoring effects. As the wind angle increases further, the increase in |r| begins to diminish, as shown in Figure 12(b) for a wind angle of 135°. When the wind angle increases to 135°, the maximum magnitude of yaw response shifts toward h/T=1.5, while at 150°, it becomes more pronounced at h/T=3, where the reduced shallow-water constraints allow the aerodynamic yaw moment to have a stronger relative contribution. Beyond these angles, variation in yaw-rate magnitude |r| gradually decreases as the aft-quartering wind becomes more aligned with the ship's longitudinal direction, reducing the effective yaw moment. When the wind acts in the opposite direction, the yaw-rate magnitude |r| exhibits its largest decrease at a wind angle of approximately 120°, with the most pronounced effect observed at h/T=1.2. At this ratio, |r| decreases to 0.44, 0.41, and 0.37, corresponding to decreases of 4.2 %, 10 %, and 19 % at wind speeds exceeding 5 m/s. These decreases become larger at lower ship speeds, reaching 7.6 %, 18.5 %, and 36.4 % with corresponding values of 0.43, 0.38, and 0.29. As the wind angle increases beyond 120°, the decrease in |r| begins to diminish gradually at all h/T ratios, as the wind shifts further toward the aft-quartering direction, as shown in Figure 12(b*) at a wind angle of 135°.

As the wind angle exceeds 90° and shifts toward the aft-quartering direction while acting in the same direction as the ship's turning motion, the drift angle magnitude gradually decreases under all h/T conditions, as shown in Figure 12(c). This reduction is associated with the decreasing lateral component of the wind force as the wind direction moves away from the beam condition. The influence of wind direction becomes less pronounced as the h/T ratio decreases, where stronger shallow water effects modify the hydrodynamic response. As the lateral wind force diminishes, the balance between aerodynamic forces and hydrodynamic restoring forces becomes the dominant factor governing the drift angle. In contrast, when the wind acts opposite to the ship's turning direction, the drift angle magnitude decreases, with the maximum reduction observed around a wind angle of approximately 120° for all h/T conditions. The reduction is pronounced at h/T=3; the drift angle reductions reach 6.7 %, 14.3 %, and 23.7 % for wind speeds above 5 m/s, with values of 15.7°, 14.4°, and 12.8°. These reductions become more significant under reduced-speed conditions, increasing to 11.5 %, 23.5 %, and 37.4 %, with corresponding drift angles of 14.9°, 12.9°, and 10.6°, respectively. This behavior results from the changing balance between wind-induced lateral forces and hydrodynamic restoring forces under different water depth conditions. As the wind angle increases further toward the aft-quartering direction, the reduction in drift angle becomes less pronounced due to the decreasing lateral component of the wind force, as shown in Figure 12(c*).

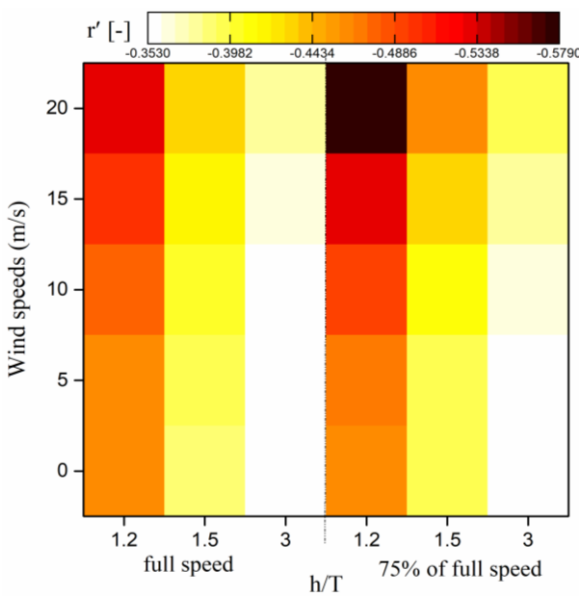
When the wind angle exceeds 120° and acts in the same direction as the ship turning, the forward speed change increases slightly at h/T=1.2 and 1.5 as the aft-directed longitudinal wind component becomes larger and partially compensates for the hydrodynamic resistance, while at h/T=3, the forward speed change becomes less sensitive to the wind direction, indicating a weaker influence of the wind-induced longitudinal force on the overall resistance balance. This behavior is governed by the interaction between the wind-induced force and the hydrodynamic resistance under different water-depth conditions, as shown in Figure 12(d). When the wind acts in the opposite direction to the ship's motion, as shown in Figure 12(d*), the increase in forward speed becomes more pronounced, with the largest effect observed at h/T=3. This behavior is attributed to the increased contribution of wind-induced resistance to the overall force balance at larger h/T ratios, where the relative influence of hydrodynamic resistance is reduced. For wind speeds above 5 m/s, the change in forward speed increases by 5.1 %, 11.6 %, and 21 %, with values of 0.44, 0.46, and 0.50, respectively. These values increase when ship speed is reduced to 75 % of full speed, reaching 9 %, 20.8 %, and 38.1 %, with corresponding values of 0.45, 0.50, and 0.57, respectively.



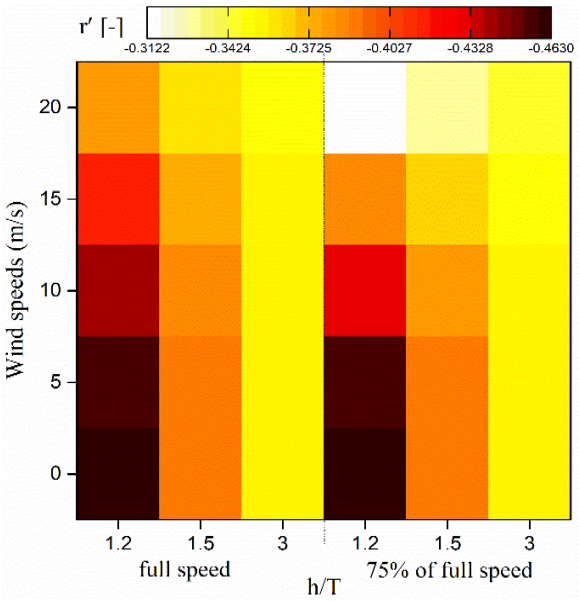
a) Turning trajectory when the wind acts in the same direction



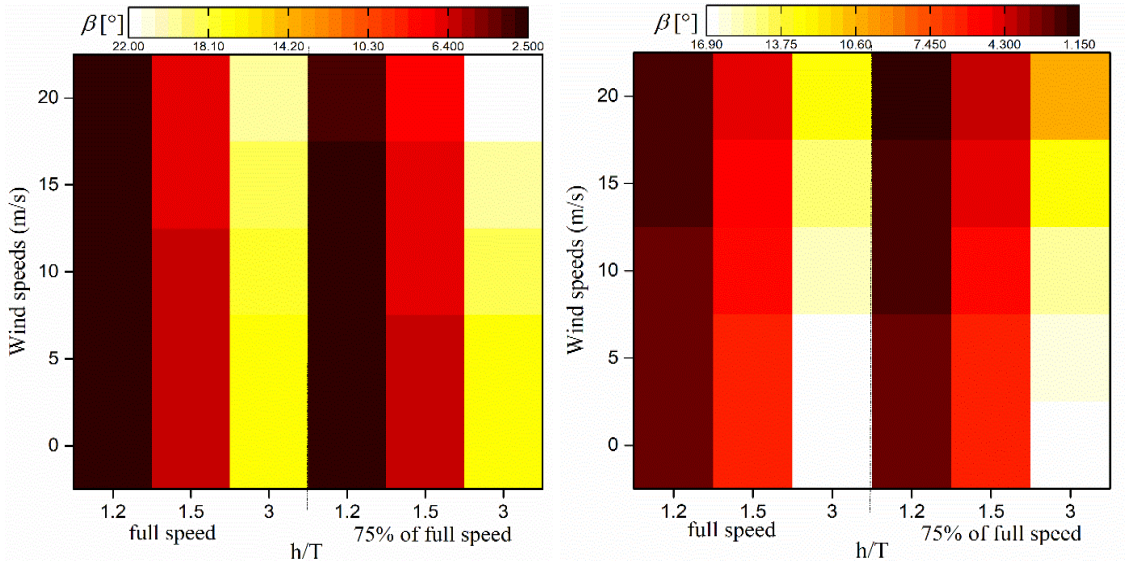
a*) Turning trajectory when the wind acts in the opposite direction



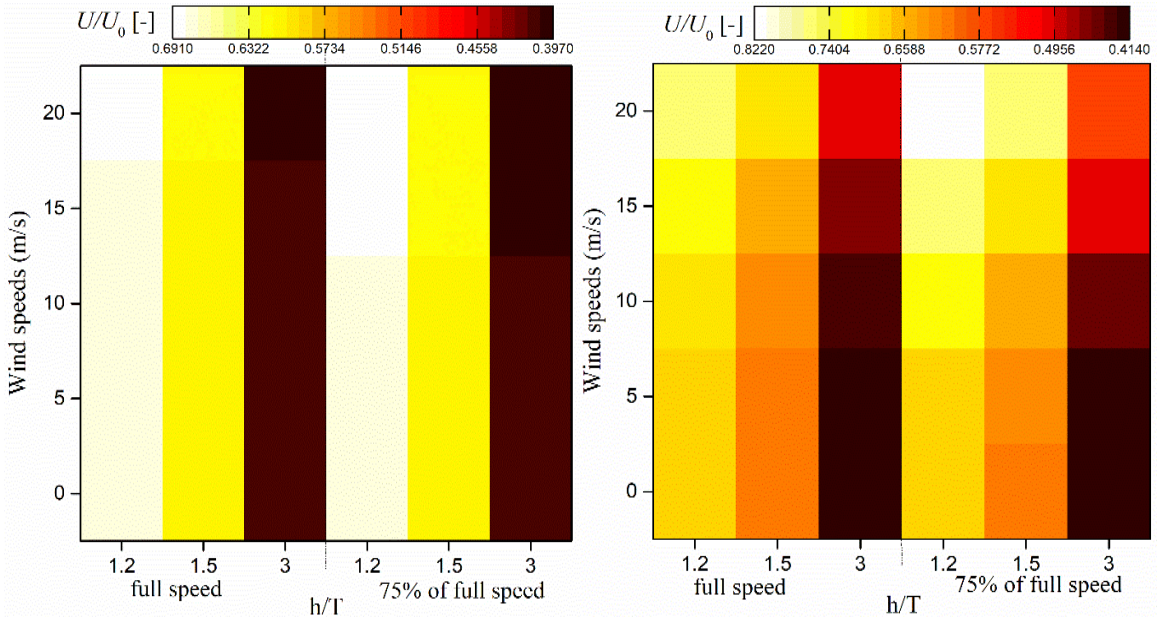
b)Yaw rate when the wind acts in the same direction



b*) Yaw rate when the wind acts in the opposite direction



c)Drift angle when the wind acts in the same direction c*) Drift angle when the wind acts in the opposite direction



d)Speed changes when the wind acts in the same direction d*) Speed changes when the wind acts in the opposite direction

Fig. 12 Comparison of turning trajectory and indices at different *h/T* ratios at full and 75 % of full ship speed for the aft-quartering wind scenarios (135°)

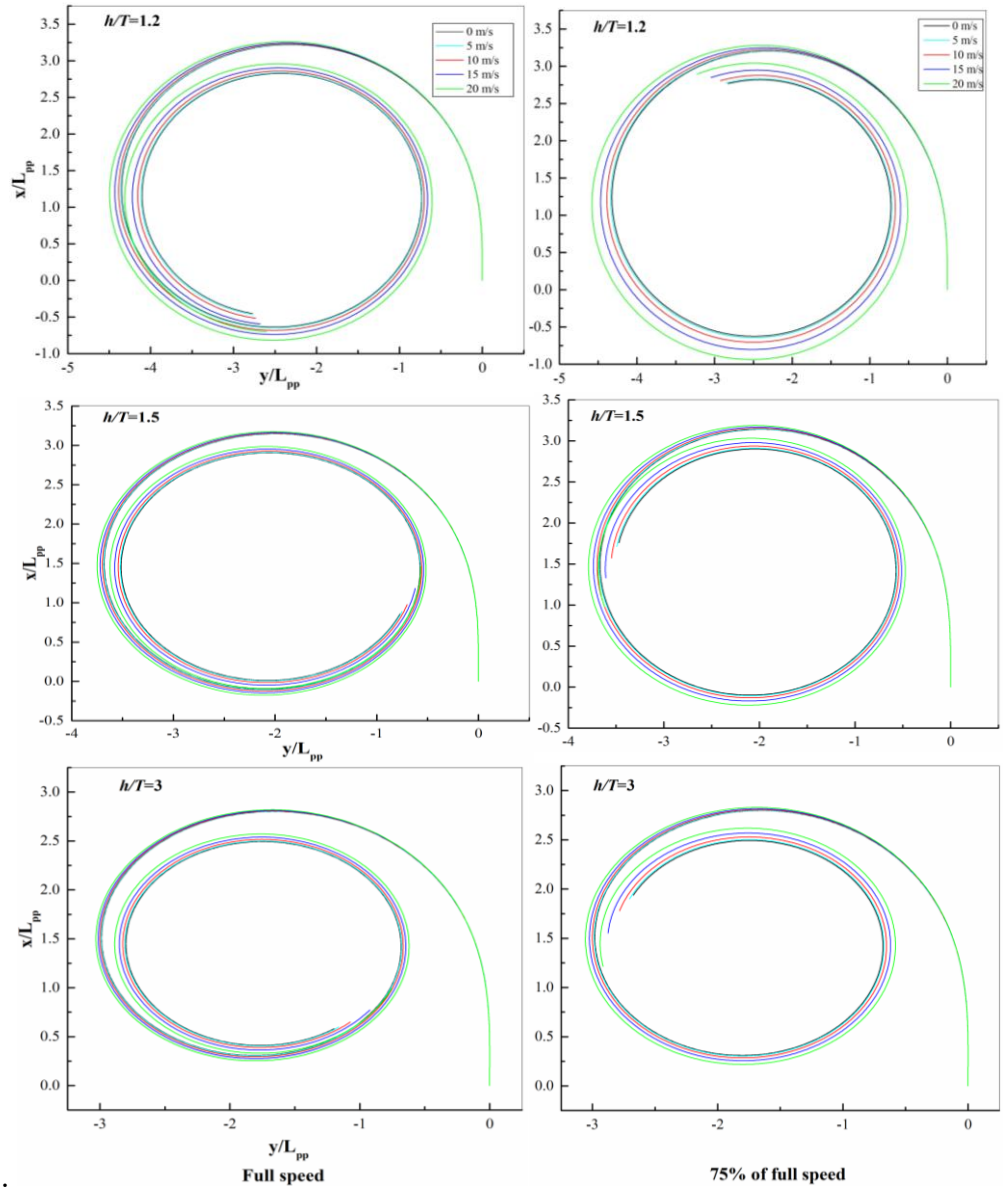
4.5 Following-wind scenarios (180°)

Under following wind conditions, as shown in Figure 13(a), the turning trajectory exhibits a slight increase in maximum advance and transfer. This effect is attributed to the longitudinal wind component, which reduces aerodynamic resistance and allows the ship to maintain a higher forward speed during maneuvering. The influence becomes more pronounced at *h/T*=1.2 and gradually decreases as the *h/T* ratio increases. At *h/T*=1.2, trajectory elongation becomes noticeable for wind speeds above 10 m/s under full-speed conditions and increases further when the ship speed is reduced to 75 % of full speed.

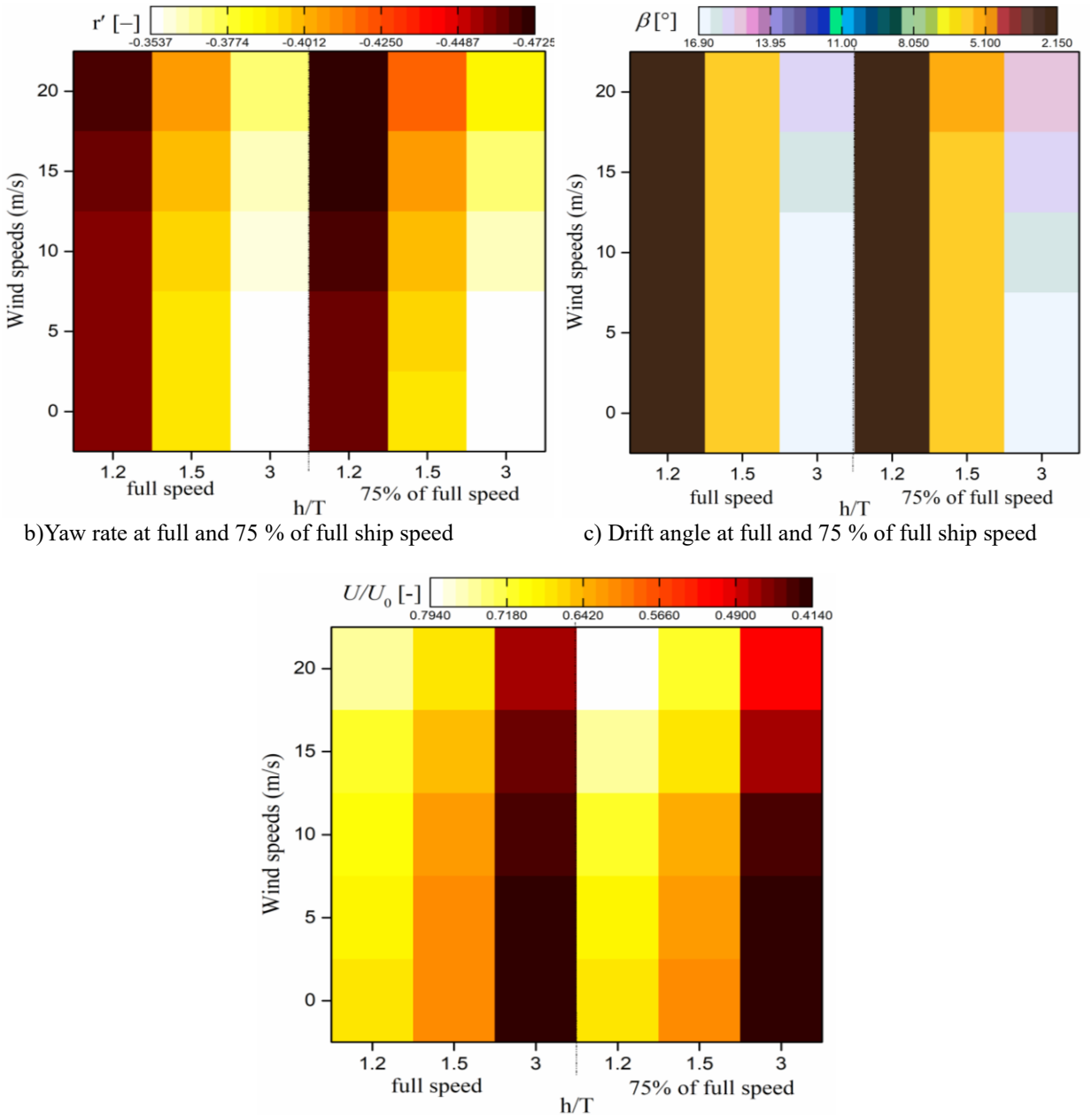
In Figure 13(b), the magnitude of yaw rate |r| increases under following wind conditions for all *h/T* ratios, with the most pronounced increase observed at *h/T*=3. The influence decreases as the *h/T* ratio decreases. At *h/T*=3, the yaw rate magnitude increases by 1.4 %, 3.1 %, and 5.5 %, with corresponding values of 0.35, 0.36, and 0.37, at wind speeds of 10, 15, and 20 m/s, respectively. These increases become more pronounced when the ship speed is reduced to 75 % of full speed, reaching 2.4 %, 5.4 %, and 9.4 %, with values of 0.36, 0.37, and 0.39. This behavior indicates that, under the following wind conditions, the wind-induced yaw moment has a greater relative influence at larger *h/T*, where the ship's hydrodynamic response becomes less restrictive to wind-induced yaw motion.

The drift angle magnitude decreases at all *h/T* ratios under the following wind conditions, as shown in Figure 13(c). This reduction results from the longitudinal wind component, which reduces the relative aerodynamic forces and limits lateral deviation during maneuvering. The effect is pronounced at *h/T*=3 and becomes less pronounced as the *h/T* ratio decreases. At *h/T*=3, the drift angle decreases by 1.7 %, 3.6 %, and 6.0 %, with corresponding values of 16.6°, 16.2°, and 15.8°, at wind speeds of 10, 15, and 20 m/s, respectively. These reductions become more pronounced when the ship speed is reduced, reaching 2.8 %, 5.9 %, and 9.5 %, with values of 16.4°, 15.9°, and 15.3°. This indicates that lower ship speed increases the sensitivity of the drift response to wind effects due to the reduced hydrodynamic resistance against wind-induced lateral motion.

In Figure 13(d), the forward speed change increases under following wind conditions for all *h/T* ratios, indicating that the positive longitudinal wind force assists the ship's forward motion and reduces the loss of surge speed during the turning maneuver. The increase is larger at *h/T*=3 and gradually decreases as the *h/T* ratio decreases. At *h/T*=3, the forward speed increases by 3.1 %, 7 %, and 12.3 %, with corresponding values of 0.43, 0.44, and 0.47, at wind speeds of 10, 15, and 20 m/s, respectively. These increases become more pronounced when the ship speed is reduced to 75 % of full speed, reaching 5.5 %, 12.2 %, and 21.2 %, with values of 0.438, 0.466, and 0.503.



a) Turning trajectory at full and 75% of full ship speed



b)Yaw rate at full and 75 % of full ship speed

c) Drift angle at full and 75 % of full ship speed

d) Forward speed change at full and 75 % of full ship speed

Fig. 13 Comparison of turning trajectory and indices at different *h/T* ratios at full and 75 % of full ship speed for the following-wind scenarios (180°)

4.6 Lateral drift and tactical diameter

Figure 14 illustrates the influence of wind direction on the lateral drift response. When the wind acts in the same direction as the ship's turning motion, the lateral drift is mainly governed by the balance between the wind-induced lateral force and the hydrodynamic restoring forces. The drift response becomes more pronounced under oblique and beam wind conditions, where the lateral component of the wind force increases. The effect is most significant at *h/T*=1.2 and gradually decreases as the *h/T* ratio increases due to decreased shallow water influence. Conversely, when the wind acts opposite to the ship's turning direction, the lateral drift becomes larger because the wind-induced yaw moment counteracts the natural turning motion, increasing the lateral deviation during maneuvering. The maximum drift response occurs under beam and quartering wind conditions, where both the lateral wind force and opposing yaw moment contribute to the increase in drift. In both wind-direction cases, reducing the ship speed to 75 % of full speed amplifies the lateral displacement response across all *h/T* ratios, as the lower forward speed reduces hydrodynamic resistance to lateral motion and increases the relative influence of wind-induced forces. These

results demonstrate that the combination of shallow water effects, reduced ship speed, and adverse wind direction significantly increases the sensitivity of lateral maneuvering performance to wind disturbances.

Figure 15 shows the effect of wind direction on the tactical diameter under different wind speeds, *h/T* ratios, and ship speeds. When the wind acts in the same direction as the ship's turning motion, the wind-induced yaw moment assists the rudder-induced turning, resulting in a reduction in tactical diameter, particularly under oblique and quartering wind conditions. Conversely, when the wind acts opposite to the turning direction, the adverse yaw moment reduces turning capability and increases the tactical diameter. The wind influence becomes more effective at lower ship speeds, where the reduced hydrodynamic forces increase the relative contribution of wind-induced moments. Overall, the tactical diameter response is governed by the balance between aerodynamic yaw moment and hydrodynamic restoring forces, with stronger sensitivity observed under beam and aft quartering wind conditions and reduced speed operations.

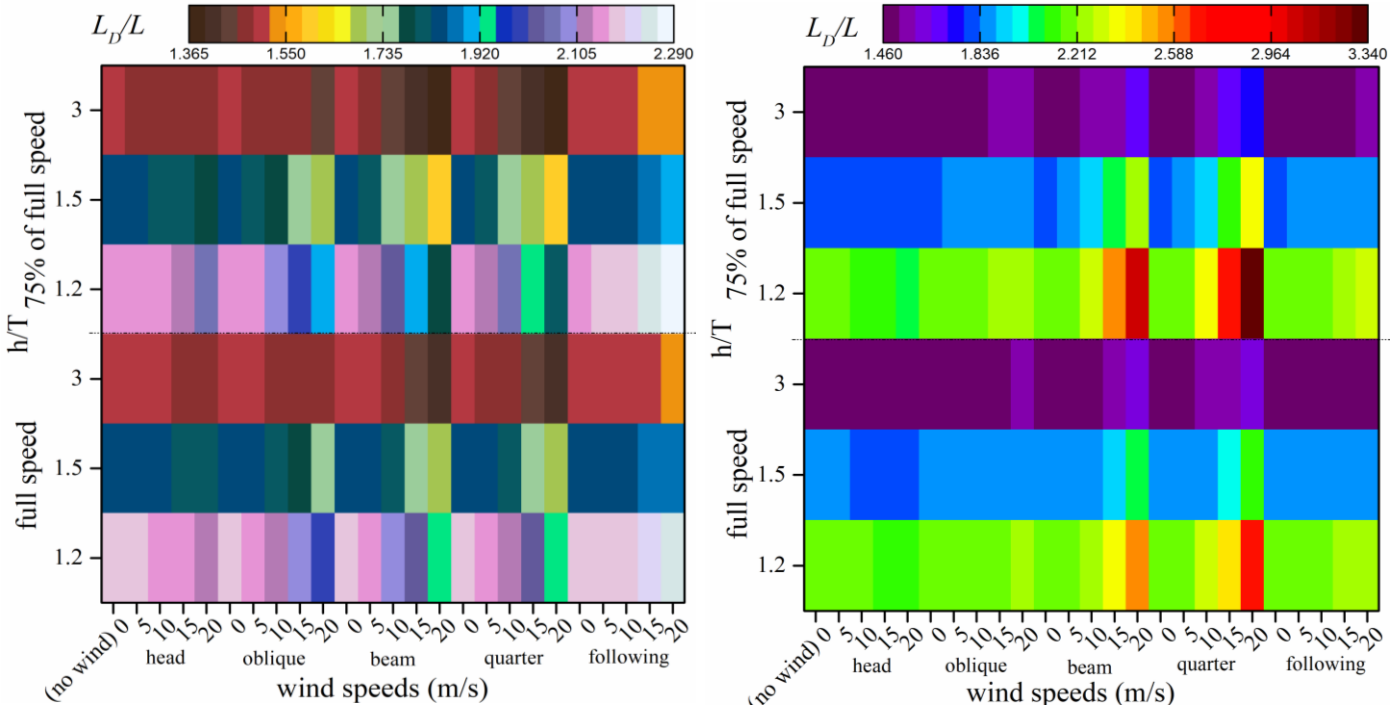


Fig. 14 Lateral drift at various wind angles, speeds, ship speed, and different *h/T* ratios in the same direction of turning (left) and in the opposite direction (right)

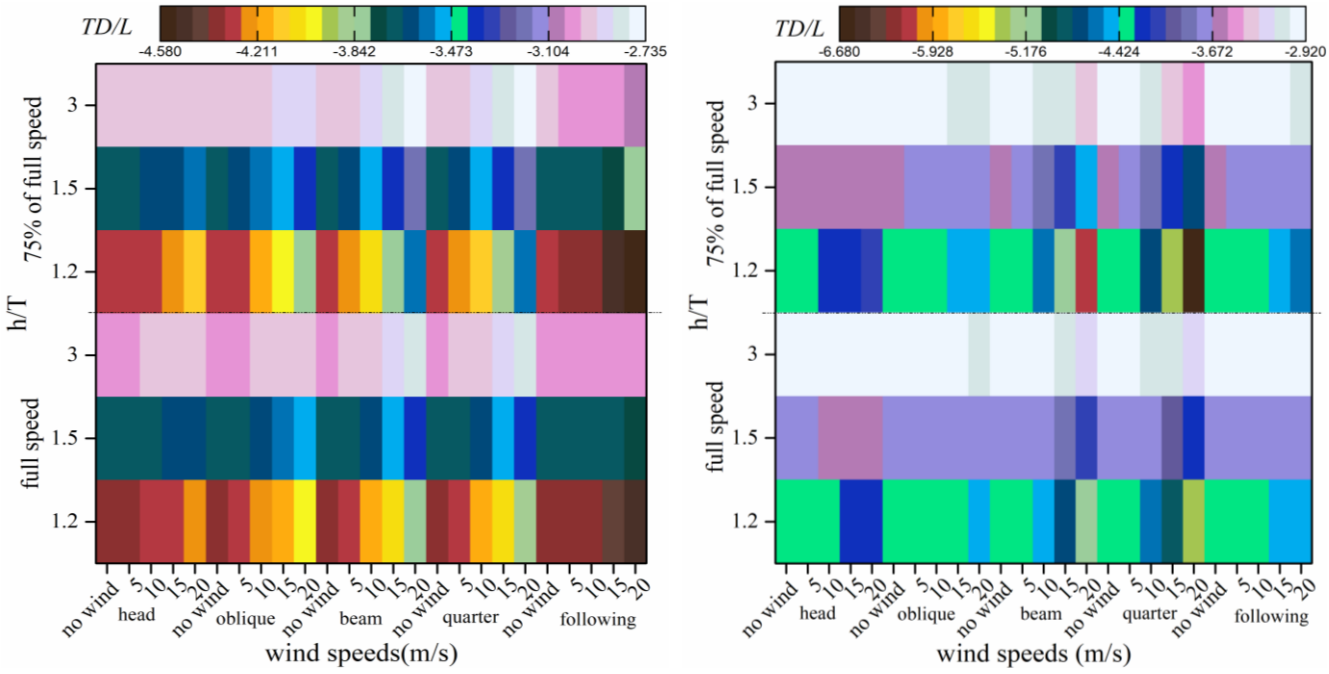


Fig. 15 Tactical diameter at various wind speeds, angles, *h/T* ratios, and ship speeds in the same direction (left) and in the opposite direction (right)

5. Sensitivity and variability

5.1 Sensitivity analysis

Morris' method is used to identify the input parameter that influences the output variables, which is known as the Elementary Effect (EE) [45, 46]. This global sensitivity analysis technique provides a qualitative assessment of input importance. It employs a trajectory-based sampling approach to estimate the standard deviation (σ), which is related to nonlinearity or interaction effects, and the absolute mean (μ^*), which represents the overall influence of an input parameter on the output. Additionally, the ratio σ/μ^* indicates the relative importance of nonlinearity and the interaction effects among input variables. One of the key advantages of this method is its ability to capture interaction effects and nonlinear (non-monotonic) relationships.

The Morris sensitivity is an index of the sensitivity of uncertain inputs. For a certain model $f(X)$ where n independent inputs (x_1, x_2, ..., x_n) are known as:

$$EE_i = \frac{f(x_1, x_2, ..., x_{i+\Delta}, x_{i+\Delta+1}, ..., x_n) - f(x)}{\Delta} \tag{24}$$

$$\mu_i^* = \frac{1}{r}\sum_{j=1}^{r}\left|EE_{i,j}\right| \tag{25}$$

$$\sigma_i = \sqrt{\frac{1}{r-1}\sum_{j=1}^{r}(EE_{i,j} - \frac{1}{r}\sum\nolimits_{j=1}^{r} EE_{i,j})} \tag{26}$$

where $EE_{i,j}$ is the j-th elementary impact of the input parameter, r is the number of trajectories, and $(EE_{i,j} - \frac{1}{r}\sum\nolimits_{j=1}^{r} EE_{i,j})$ is the mean of elementary effects. The sensitivity indices are reported as non-normalized values calculated directly from the simulated maneuvering responses, as different outputs have different magnitudes. The Morris sampling design used 50 optimal trajectories with four input variables (wind speed, wind angle, *h/T*, and ship speed) and six levels selected to discretize each input variable and maximize space coverage. The step size $\Delta = \text{levels}/(2(\text{levels}-1)$ is determined according to the Morris grid definition. The convergence of the Morris results is verified by increasing the number of trajectories until the ranking of the dominant parameters remains unchanged, indicating convergence of the results. The four input variables considered in the Morris analysis are wind speed, wind angle, (*h/T*), and ship speed. Among these, *h/T* and ship speed are available at discrete conditions in the simulation database: *h/T* takes the values 1.2, 1.5, and 3.0, and ship speed takes the values 100 % and 75 % of full speed. The Morris trajectories are generated over the normalized bounds of the four input variables using six grid levels. Because the sensitivity analysis is performed using the existing simulation database rather than by executing the maneuvering model at every Morris sample, each sampled point is mapped to the nearest available combination in the simulation database using Euclidean distance. The corresponding simulated response is then used to calculate the elementary effects. Thus, the reported Morris indices provide a screening assessment based on the available discrete simulation cases.

Table 7 shows the values of standard deviation σ and absolute mean μ^* for input parameters affecting output, including yaw rate, drift angle, and speed change in both directions. The Morris analysis shows that *h/T* significantly influences the maneuvering indices, particularly yaw rate and drift angle. The ratio σ/μ^* for *h/T* is low, indicating that its effect is primarily linear (monotonic), but the magnitude of μ^* confirms that it is an important parameter.

Figures 16(a) and (b) present the ratio σ/μ^*, which characterizes the relative contribution of nonlinear and/or interaction effects to the elementary-effect variability. The overall influence is assessed using μ^*, whereas σ represents the dispersion of the elementary effects associated with nonlinearity and/or interactions. The value of the σ/μ^* ratio indicates a predominantly linear effect when (σ/μ^* <1) or a nonlinear and interactive effect when (σ/μ^* >1). In Figure 16(a), the σ/μ^* ratio for ship speed exceeds 1 for drift angle,

indicating that nonlinear and/or interaction effects are important relative to its overall effect. A similar tendency is observed in Figure 16(b). The depth-to-draft ratio (h/T) shows (σ/μ^* <1), indicating a predominantly linear (monotonic) effect, except for yaw rate, where σ/μ^* approaches 1, indicating a transitional behavior between linear and nonlinear. The wind angle exhibits relatively high σ/μ^* values, particularly for drift angle in Figure 16(b), indicating substantial nonlinear and/or interaction contributions. A similar tendency is observed in Figure 16(a), with notable σ/μ^* values for yaw rate and drift angle, indicating nonlinearity due to variations in force and moment with the relative wind direction. Wind speed shows moderate σ/μ^* values in Figure 16(b) compared to Figure 16(a), indicating a comparatively lower relative contribution of nonlinear and/or interaction effects except for the forward speed change.

Table 7 Morris sensitivity analysis results for ship maneuvering response parameters

parameters	same direction						opposite direction					
	yaw rate		drift angle		speed change		yaw rate		drift angle		speed change	
	σ	μ^*	σ	μ^*	σ	μ^*	σ	μ^*	σ	μ^*	σ	μ^*
ship speed	0.0108	0.0071	1.4679	0.8941	0.031	0.0215	0.0123	0.0092	1.2859	0.671	0.0329	0.0216
h/T	0.0498	0.079	3.1275	18.7326	0.049	0.3258	0.0423	0.0893	2.5147	17.1496	0.0496	0.3051
wind angle	0.0361	0.0195	4.2723	2.3909	0.0773	0.062	0.0185	0.0147	3.3178	1.9531	0.0897	0.06297
wind speed	0.018	0.0124	2.09981	1.6742	0.0457	0.0408	0.0226	0.0193	1.7153	1.394	0.0556	0.0458

5.2 Bootstrap-based variability assessment

In this study, the bootstrap method is employed to characterize the sampling behavior of the mean response computed over the pooled simulation dataset. The bootstrap analysis evaluates how the estimated mean of the pooled response varies across resampled datasets, providing a measure of the sampling variability and precision of the estimated mean across the full set of investigated cases, particularly for nonlinear relationships in small datasets, without requiring assumptions about the data distribution. This method estimates variability, confidence intervals, standard errors, and other measures to characterize the sampling behavior of the estimated mean of the pooled simulation outputs and is not a direct measure of scenario-to-scenario dispersion or a probabilistic model of physical or model uncertainty. Moreover, it provides a robust estimate even for multiple input and output variables [47]. The bootstrap variability assessment is performed using the complete simulation database consisting of 780 numerical cases. Resampling the available simulation outputs is performed using a total of 1300 samples. The 95 % confidence interval of the bootstrap mean is obtained using the percentile method. The standard deviation of the bootstrap statistics represents the sampling variability of the estimated response mean across resampled datasets. Additionally, the Shapiro-Wilk test is used to assess the normality of the bootstrap-mean distributions [48]. For all outputs, the *p*-values are greater than 0.05, indicating that normality is not rejected at the 5 % significance level. This result supports using the percentile method for the confidence intervals.

Figure 17 displays the bootstrap histogram distributions of the estimated mean responses for yaw rate, drift angle, and forward speed change. In Figure 17(a), the yaw rate shows a mean of 0.4112 and a standard deviation of 0.0029, indicating low sampling variability; the narrow confidence interval (CI) of (0.4172, 0.4057) confirms the low sampling variability of the estimated mean. The drift angle shows a higher mean of 9.1997 and a relatively large standard deviation of 0.3538, indicating greater sensitivity to variations across the investigated scenarios; the CI of (8.5058, 9.9211) is correspondingly wider, reflecting the ship's limited ability to resist aerodynamic lateral forces. The mean speed change is 0.5586 with a standard deviation of 0.0060, indicating that the ship decelerates under wind effects due to increased drag; the narrow confidence interval (0.5462, 0.5705) indicates low sampling variability. The Skewness and excess Kurtosis values are close to zero for all output variables, which is consistent with the Shapiro–Wilk results for the bootstrap-mean distributions. In Figure 17(b), the yaw rate (mean=0.3910, standard deviation=0.0021, CI = (0.3951, 0.3870)) and speed change (mean=0.5847, standard deviation=0.0056, CI = (0.5742, 0.5955)) show small standard deviations and narrow CI ranges, confirming low sampling variability. In contrast, the drift

angle shows a relatively high standard deviation of 0.2790 and a wide CI of (7.2589, 8.3335), indicating substantial variability.

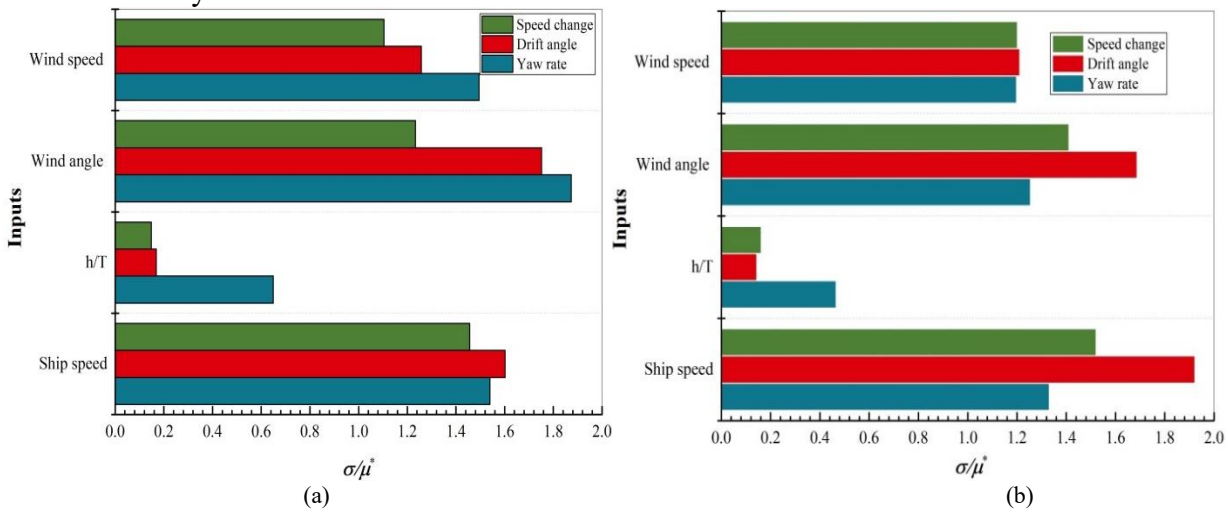
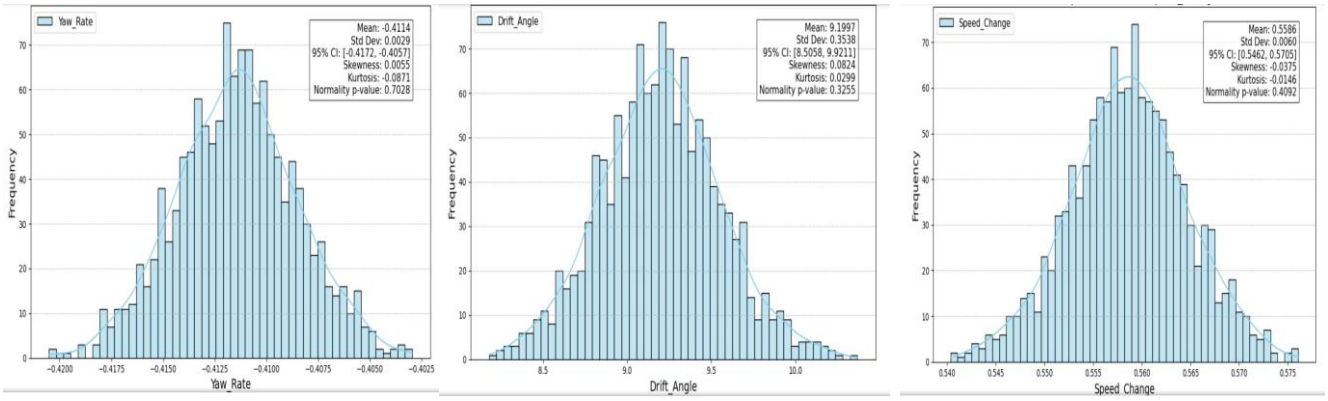
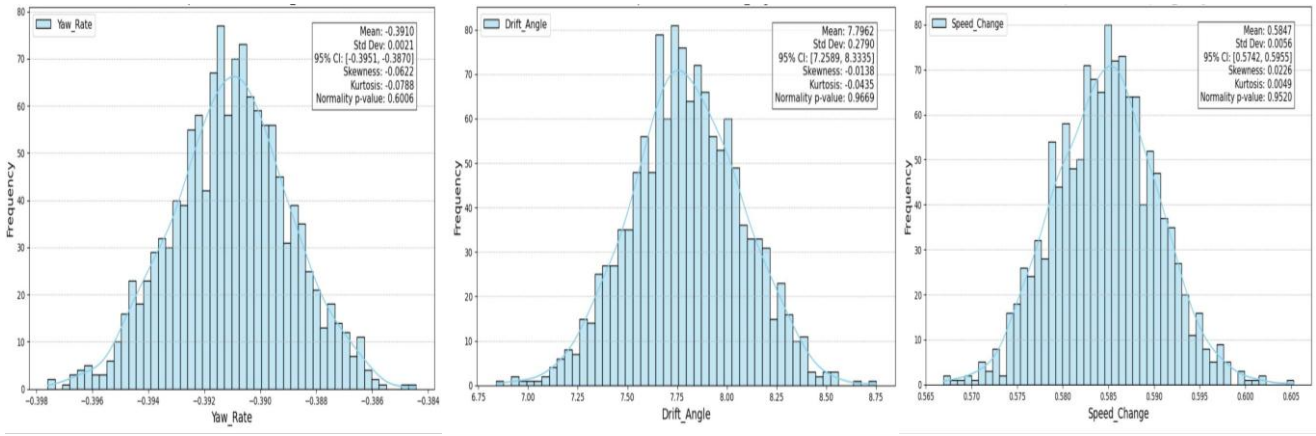


Fig. 16 Morris sensitivity analysis of the influence of input variables on the output variables when the wind acts in the same direction (a) and in the opposite direction (b)



a) The output variability when the wind acts in the same direction as the ship turning



b) The output variability when the wind acts in the opposite direction to the ship turning

Fig. 17 The variability of the output variables when the wind acts in both directions

6. Conclusion

This study investigates ship turning maneuvering under a combination of shallow water and wind disturbances. Based on the MMG mathematical model, a modular maneuvering model is developed to evaluate the trajectory characteristics and maneuvering indices of the KVLCC2 benchmark hull under different operational conditions, including ship speed, depth-to-draft ratio (*h/T*), wind speed, and wind

direction, which are systematically evaluated. Based on the findings, some concluding remarks from the safety perspective are drawn as follows:

- The shallow water effects significantly modify ship maneuvering characteristics by changing the hydrodynamic force and moment balance. Among the investigated parameters, the depth-to-draft ratio (*h/T*) strongly influences the turning response, with the strongest effects observed under extreme shallow-water conditions (*h/T*=1.2). The influence of wind disturbances becomes more pronounced as the water depth decreases.
- Wind forces produce small changes in turning trajectories, yaw rate response, drift angle, and forward speed change in some cases. The present model describes changes of the order of 1-4 % as small or marginal predicted trends rather than as quantitatively significant changes. The magnitude and direction of these effects depend strongly on the relative wind direction because the aerodynamic sway force and yaw moment vary with the wind angle relative to the ship. Higher wind speeds within the investigated range (5–20 m/s) lead to larger deviations from the corresponding no-wind baseline cases, particularly under extreme shallow water conditions.
- Reducing ship speed increases the relative contribution of aerodynamic forces to the total maneuvering force balance because the hydrodynamic forces decrease with ship speed. Consequently, reduced speed cases show stronger wind-induced variations in trajectory and lateral motion. However, the appropriate operational speed in practical navigation should be determined considering the complete navigation environment, including traffic conditions, under-keel clearance (UKC), heel angle, roll response, trim variation, maneuvering requirements, and the master's risk assessment.
- The influence of environmental conditions is not identical for all maneuvering indices. The trajectory characteristics (advance, transfer, tactical diameter) and yaw response are more sensitive under extreme shallow water conditions *h/T*=1.2, while drift angle and speed variations become more significant under other combinations of water depth and wind conditions. These results highlight that different maneuvering criteria such as trajectory deviation, yaw stability, drift angle, and speed loss should be considered when evaluating ship behavior in shallow water.
- The Morris sensitivity analysis indicates that the depth-to-draft ratio (*h/T*) is one of the most influential parameters affecting the predicted maneuvering responses. Wind-related parameters mainly contribute to variations in aerodynamic response and nonlinear interactions. The bootstrap-based variability assessment shows that drift angle exhibits the largest dispersion among the investigated scenarios, indicating that lateral motion prediction is more sensitive to changes in operating and environmental conditions.

The present study is limited to the KVLCC2 benchmark hull under steady wind conditions using a 3-DOF MMG maneuvering model. The aerodynamic forces are treated as constant for each prescribed steady wind condition. The apparent wind and aerodynamic forces are not updated using the instantaneous ship heading and velocity during the integration. Therefore, time-varying aero-hydrodynamic coupling is not represented in the present model. Effects of wind gusts, waves, currents, bank interaction, loading-condition variations, roll coupling, and dynamic trim/squat are not considered. The fixed-draft assumption may influence the prediction of hydrodynamic and aerodynamic interactions in shallow water. In addition, the wind-affected maneuvers are not directly validated due to the lack of available experimental datasets. Future work will focus on incorporating dynamic sinkage and trim, higher-degree-of-freedom motion models, and validation for different ship types and environmental conditions to improve the applicability of the approach. Moreover, the Raven shallow-water resistance correction is applied beyond the ITTC applicability conditions at *h/T*=1.5 and 1.2; therefore, the results at these very shallow-water conditions require further validation against experimental or high-fidelity numerical data. Consequently, interpret the results at *h/T*=1.2 and 1.5 as model predictions rather than fully validated quantitative results. Independent experimental or CFD validation at these extreme shallow-water conditions remains desirable and is recommended for future work.

ACKNOWLEDGMENTS

This work is supported by the Ministry of Science and Technology of China (Grant No. 2025YFE0125300. The work is also supported by the National Natural Science Foundation of China (Grant No. 51779055). The first author is supported by the Marine Scholarship of China (2022SOA013398).

NOMENCLATURE

Symbol	Description		
CFD	Computational Fluid Dynamics	v'	Non-dimensional sway velocity
EFD	Experimental Fluid Dynamics	t_p	Thrust deduction factor
DOF	Degree of Freedom	L / L_{pp}	Length between perpendiculars
MMG	Maneuvering Modeling Group	I_{zz}	Moment of inertia
SVM	Support Vector Machine	K_T	Propeller thrust coefficient
h/T	Depth-to-draft ratio	r'	Non-dimensional yaw rate
AIS	Automatic Identification System	t'	Non-dimensional time
x_G	Longitudinal center of gravity	ITTC	International Towing Tank Conference
ψ_w,ψ_{aw}	True and apparent wind angle	T	Ship draft
U_w, U_{aw}	True and apparent wind velocities	h	Water depth
ψ	Heading angle	x_R,x_H	Longitudinal references of the rudder location
O_0	Pivot point of Earth coordinates	A_R	Rudder area
δ_R	Rudder angle	D_p	Propeller diameter
β	Drift angle	CI	Confidence interval
r	Yaw rate	F_N	Rudder normal force
m	Ship mass	μ^*	Absolute mean
u, v	Ship velocities in x and y axes	σ	Standard deviation
$\dot{u},\dot{v},\dot{r}$	Surge, sway and angular acceleration	n_p	Propeller rotation frequency
X_H, Y_H, N_H	Surge, lateral, and yaw forces of hull	t_R	Reduction factor of steering resistance
X_R, Y_R, N_R	Rudder forces	J_P	Advance ratio
X_P	propeller force	w_P	Wake fraction
X_E, Y_E, N_E	External wind forces	k_2,k_1,k_0	Approximating coefficients
ρ	Density of water	kn	knot
a_H	Rudder force increase coefficient	[-]	Means the non-dimensionalization

P, R, H, E	Subscripts for propeller, rudder, hull, and external forces	m/s	meter per second
U	Ship speed at midship	f_a	Rudder lift gradient coefficient
$C_{T\,shallow}$	Viscous resistance coefficient in shallow water	a_R	Attack angle
R_0'	Ship resistance	U_R	Rudder velocity
S_W	Wetted surface area of hull	C_F	Frictional resistance
C_T	Drag coefficient	C_W	Wave resistance coefficient
ΔC_F	Roughness drag coefficient	k_s	Average hull surface roughness
η	Ratio of propeller diameter to rudder span	u_R, v_R	Rudder surge and sway forces
ε	Ratio of wake fraction	κ	Empirical constant
γ_R	Flow straightening coefficient	β_R	Effective rudder inflow angle
ρ_A	Air density	L_{OA}	Ship length overall
C_X, C_Y, C_N	Aerodynamic coefficients	A_L, A_F	Lateral and frontal projected areas
$V_{W_{(E)}}$	True wind velocity vector in the Earth-fixed frame	U_0	Initial ship speed
$V_{S_{(E)}}$	ship's velocity in the Earth-fixed coordinate	°/s	Degree per second
$V_{aw_{(E)}}$	Apparent wind velocity vector in the Earth-fixed coordinate	B	Breadth of ship
k_{zz}	Radius of gyration	∇	Ship displacement
A_w	Waterplane area	C_B	Block coefficient
U/U_0	Speed change	max(Y)	Maximum lateral displacement due to the change in ship heading
AD	Advance	L_D	Lateral drift
TR	Transfer	$EE_{i,j}$	j-th elementary impact of the input parameter
r	Number of trajectories	Δ	step size
$X_0, X_1, X_3, X_5, Y_1, Y_3, Y_5, N_1, N_2, N_3$	Regression parameters	$\mu_{11}, \mu_{22}, \mu_{66}, \mu_{62}, \mu_{26}$	Added mass derivatives
t_{90}, t_{180}	Times when the change in heading reaches 90° and 180°	x_0, y_0	Initial position on ship
|r|	yaw-rate magnitude		

APPENDIX A: Empirical Formulas for Ship Hydrodynamic Coefficients

A1: Empirical Formulas for Hydrodynamic Coefficients of Inertia

$$X_{\dot{u}} = \frac{\partial X}{\partial \dot{u}} = \frac{m}{\pi\sqrt{\frac{L^3}{\nabla}} - 14} \quad [29] \tag{A1}$$

$$Y_{\dot{v}} = \frac{\partial Y}{\partial \dot{v}} = 0.5\rho L^3 \left(-\pi \left(\frac{T}{L} \right)^2 \left(1 + 0.16 \left(\frac{C_B B}{T} \right) - 5.1 \left(\frac{B}{L} \right)^2 \right) \right) \quad [30] \tag{A2}$$

$$Y_{\dot{r}} = \frac{\partial Y}{\partial \dot{r}} = 0.5\rho L^4 \left(-\pi \left(\frac{T}{L} \right)^2 \left(0.67 \left(\frac{B}{L} \right) - 0.0033 \left(\frac{B}{T} \right)^2 \right) \right) \quad [30] \tag{A3}$$

$$N_{\dot{v}} = \frac{\partial N}{\partial \dot{v}} = Y_{\dot{r}} \quad [30] \tag{A4}$$

$$N_{\dot{r}} = \frac{\partial N}{\partial \dot{r}} = 0.5\rho L^5 \left(-\pi \left(\frac{T}{L} \right)^2 \left(0.0833 + 0.017 \left(\frac{C_B B}{T} \right) - 0.0033 \left(\frac{B}{L} \right) \right) \right) \quad [30] \tag{A5}$$

A1.1 Empirical formula for viscous hydrodynamic coefficients of ships

A1.1.1 Empirical formula for longitudinal viscous hydrodynamic coefficients

$$X'_{vv} = \left[\frac{1.15 C_B B}{L} - 0.18 \right] \frac{T}{L} \quad [33] \tag{A6}$$

$$X'_{vvvv} = \left[-\frac{6.68 C_B B}{L} + 1.1 \right] \frac{T}{L} \quad [33] \tag{A7}$$

$$X'_{rr} = \left[-\frac{0.085 C_B B}{L} + 0.008 + \frac{x'_G Y'_{\dot{v}}}{T} \right] \frac{T}{L} \quad [33] \tag{A8}$$

$$X'_{vr} = \left[0.117 Y'_{\dot{v}} \left(0.5 + C_B \right) \right] \quad [34] \tag{A9}$$

A1.1.2 Empirical formula for transverse viscous hydrodynamic coefficients

$$Y'_{v} = -\pi \left(\frac{T}{L} \right)^2 \left(1 + \frac{0.4 C_B B}{T} \right) \quad [30] \tag{A10}$$

$$Y'_{vvv} = \left[-0.6469 \left(1 - C_B \right) \left(\frac{T}{B} \right) + 0.0027 \right] \quad [34] \tag{A11}$$

$$Y'_{r} = -\pi \left(\frac{T}{L} \right)^2 \left(-0.645 + 0.38 \frac{C_B B}{\pi T} \right) \quad [36] \tag{A12}$$

$$Y'_{rrr} = \left(-\frac{0.023 C_B T}{B} + 0.0063 \right) \quad [34] \tag{A13}$$

$$Y'_{vvr} = \left[\frac{1.5 T C_B}{B} - 0.65 \right] \frac{T}{L} \quad [35] \tag{A14}$$

$$Y'_{vrr} = -\left(5.95 \left(1 - C_B \right) \frac{T}{B} \right) \frac{T}{L} \quad [35] \tag{A15}$$

A.1.1.3 Empirical formula for viscous hydrodynamic coefficients of moment

$$N'_v = -\pi\left(\frac{T}{L}\right)^2\left(0.5+\frac{2.4T}{L}\right) \quad [30] \tag{A16}$$

$$N'_{vvv} = \left(0.0348-0.5283\left(1-CB\right)\frac{T}{B}\right) \quad [34] \tag{A17}$$

$$N'_r = -\pi\left(\frac{T}{L}\right)^2\left(\frac{1.3192}{\pi}-\frac{0.68228C_B}{\pi}-\frac{0.00019}{\pi}\frac{L^2}{T^2}\right) \quad [37] \tag{A18}$$

$$N'_{rrr} = \left[\frac{0.25C_BB}{L}-0.056\right]\frac{T}{L} \quad [33] \tag{A19}$$

$$N'_{vvr} = -\left(57.5\left(\frac{C_BB}{L}\right)^2-18.4\frac{C_BB}{L}+1.6\right)\frac{T}{L} \quad [35] \tag{A20}$$

$$N'_{vrr} = 0.5\frac{C_BT}{B}-0.05\left(\frac{T}{L}\right) \quad [33] \tag{A21}$$

APPENDIX B: Empirical Formulas for Shallow Water Correction of Ship Hydrodynamic Coefficients

B.1 Shallow Water Correction Formula for Ship Inertial Hydrodynamic Coefficients

$$X_{\dot{u}\text{Shallow}} = \left(1+\frac{3.77+1.14\frac{B}{T}-0.233\frac{L}{T}-3.43CB}{\left(\frac{h}{T}-1\right)^{1.30}}\right)X_{\dot{u}\text{Deep}} \quad [39] \tag{B1}$$

$$Y_{\dot{v}\text{Shallow}} = \left(1+\frac{0.413+0.032\frac{B}{T}+0.0129\left(\frac{B}{T}\right)^2}{\left(\frac{h}{T}-1\right)^{0.82}}\right)Y_{\dot{v}\text{Deep}} \quad [39] \tag{B2}$$

$$Y_{\dot{r}\text{Shallow}} = gv\times Y_{\dot{r}\text{Deep}} \quad [38] \tag{B3}$$

$$N_{\dot{r}\text{Shallow}} = \left(1+\frac{0.413+0.0192\frac{B}{T}+0.00554\left(\frac{B}{T}\right)^2}{\left(\frac{h}{T}-1\right)^{0.82}}\right)N_{\dot{r}\text{Deep}} \quad [39] \tag{B4}$$

$$N_{\dot{r}\text{Shallow}} = gv\times N_{\dot{r}\text{Deep}} \quad [38] \tag{B5}$$

B.1.1 Shallow water correction formula for ship viscosity hydrodynamic coefficients

B.1.1.1 Longitudinal viscous hydrodynamic coefficient shallow water correction formula as per Ankudinov et al. [38].

$$X_{vv\text{Shallow}} = fyv\times X_{vv\text{Deep}} \tag{B6}$$

$$X_{vvvv\text{Shallow}} = fyv\times X_{vvvv\text{Deep}} \tag{B7}$$

$$X_{rr\text{Shallow}} = fnr \times X_{rr\text{Deep}} \tag{B8}$$

$$X_{vr\text{Shallow}} = fyr \times X_{vr\text{Deep}} \tag{B9}$$

where the expressions fyv, fnr, and fyr are given in section B.2.

B 1.1.2 Shallow Water Correction Formula for Lateral Viscous Hydrodynamic Coefficients as per Kijima et al. [35], Vantorre [40], and Ankudinov et al. [38].

$$Y_{v\text{Shallow}} = \left(-T_H + \frac{1}{\left(1-T_H\right)^{\frac{0.4C_B B}{T}}} \right) Y_{v\text{Deep}} \tag{B10}$$

$$Y_{vvvShallow} = fyv \times Y_{vvv\text{Deep}} \tag{B11}$$

$$Y_{r\text{Shallow}} = \left(1 + A_{1_{Y_r}} T_H + A_{2_{Y_r}} T_H^2 + A_{3_{Y_r}} T_H^3\right) Y_{r\text{Deep}} \tag{B12}$$

$$Y_{rrr\text{Shallow}} = gnr \times Y_{rrr\text{Deep}} \tag{B13}$$

$$Y_{vvr\text{Shallow}} = fyv \times Y_{vvr\text{Deep}} \tag{B14}$$

$$Y_{vrr\text{Shallow}} = fyv \times Y_{vrr\text{Deep}} \tag{B15}$$

where T_H, fyv, $A_{1_{Y_r}}$, $A_{2_{Y_r}}$, $A_{3_{Y_r}}$, gnr, and fyv are given in section B.2.

B 1.1.3 Shallow Water Correction Formula for Viscous Hydrodynamic Coefficients of moment ([35, 40, 38])

$$N_{v\text{Shallow}} = fnv \times N_{v\text{Deep}} \tag{B16}$$

$$N_{vvv\text{Shallow}} = fyv \times N_{vvv\text{Deep}} \tag{B17}$$

$$N_{r\text{Shallow}} = \left(-T_H + \frac{1}{\left(1-T_H\right)^{\frac{-14.28T}{L}+1.5}} \right) N_{r\text{Deep}} \tag{B18}$$

$$N_{rrr\text{Shallow}} = gnr \times N_{rrr\text{Deep}} \tag{B19}$$

$$N_{vvr\text{Shallow}} = \left(1 + A_{1_{N_{vvr}}} T_H + A_{2_{N_{vvr}}} T_H^2 + A_{3_{N_{vvr}}} T_H^3\right) N_{vvr\text{Deep}} \tag{B20}$$

$$N_{vrr\text{Shallow}} = \left(1 + A_{1_{N_{vrr}}} T_H + A_{2_{N_{vrr}}} T_H^2 + A_{3_{N_{vrr}}} T_H^3\right) N_{vrr\text{Deep}} \tag{B21}$$

where fnv fyv, T_H, gnr, $A_{1_{N_{vvr}}}$, $A_{2_{N_{vvr}}}$, $A_{3_{N_{vvr}}}$, $A_{1_{N_{vrr}}}$, $A_{2_{N_{vrr}}}$, and $A_{3_{N_{vrr}}}$ are given in section B.2.

B.2 Formula Expressions

$$gv = K_0 + \frac{2}{3} K_1 \frac{B_1}{T} + \frac{8}{15} K_2 \left(\frac{B_1}{T}\right)^2 \tag{B22}$$

$$gnr = K_0 + \frac{8}{15} K_1 \frac{B_1}{T} + \frac{40}{105} K_2 \left(\frac{B_1}{T}\right)^2 \tag{B23}$$

$$fyr = K_0 + \frac{2}{5} K_1 \frac{B_1}{T} + \frac{24}{105} K_2 \left(\frac{B_1}{T}\right)^2 \tag{B24}$$

$$frv = K_0 + K_1 \frac{B_1}{T} + K_2 \left(\frac{B_1}{T} \right)^2 \tag{B25}$$

$$frr = K_0 + \frac{1}{2} K_1 \frac{B_1}{T} + \frac{1}{3} K_2 \left(\frac{B_1}{T} \right)^2 \tag{B26}$$

$$fyv = 1.5\, fnr - 0.5 \tag{B27}$$

$$fnr = K_0 + \frac{1}{2} K_1 \frac{B_1}{T} + \frac{1}{3} K_2 \left(\frac{B_1}{T} \right)^2 \tag{B28}$$

$$fnv = K_0 + K_1 \frac{B_1}{T} + K_2 \left(\frac{B_1}{T} \right)^2 \tag{B29}$$

$$\begin{aligned} K_0 &= 1 + \frac{0.0775}{H_T^2} - \frac{0.011}{H_T^3} + \frac{0.000068}{H_T^5} \\ K_1 &= -\frac{0.0643}{H_T} + \frac{0.0724}{H_T^2} - \frac{0.0113}{H_T^3} + \frac{0.0000767}{H_T^5} \\ &\begin{cases} K_2 = \dfrac{0.137}{H_T} \dfrac{B}{T} H_T & \text{if} \quad \dfrac{B}{T} > 4 \\ K_2 = \dfrac{0.0342}{H_T} & \text{else} \end{cases} \end{aligned} \tag{B30}$$

$$\begin{aligned} B_1 &= C_B B \left(1 + \frac{B}{L} \right)^2 \\ B_2 &= 0.83 \frac{B_1}{C_B} \end{aligned} \tag{B31}$$

$$\begin{aligned} H_T &= h / T - 1 \\ T_H &= T / h \end{aligned} \tag{B32}$$

$$\begin{aligned} A_{1_{Y_r}} &= -5.5 \left(\frac{C_B B}{T} \right)^2 + 26 \frac{C_B B}{T} - 31.5 \\ A_{2_{Y_r}} &= 37 \left(\frac{C_B B}{T} \right)^2 - 185 \frac{C_B B}{T} + 230 \\ A_{3_{Y_r}} &= -38 \left(\frac{C_B B}{T} \right)^2 + 197 C_B \frac{B}{T} - 250 \end{aligned} \tag{B33}$$

$$\begin{aligned} A_{1_{Y_{rr}}} &= -15600 (1 - C_B)^5 \\ A_{2_{Y_{rr}}} &= 116000 (1 - C_B)^5 \\ A_{3_{Y_{rr}}} &= -128000 (1 - C_B)^5 \end{aligned} \tag{B34}$$

$$\begin{aligned} A_{1_{N_{vvr}}} &= 91 C_B \frac{T}{B} - 25 \\ A_{2_{N_{vvr}}} &= -515 C_B \frac{T}{B} + 144 \\ A_{3_{N_{vvr}}} &= 508 C_B \frac{T}{B} - 143 \end{aligned} \tag{B35}$$

$$A_{1_{N_{vrr}}} = 40C_B\frac{B}{T} - 88$$
$$A_{2_{N_{vrr}}} = -295C_B\frac{B}{T} + 645 \quad \text{(B36)}$$
$$A_{3_{N_{vrr}}} = 312C_B\frac{B}{T} - 678$$

APPENDIX C: Empirical Formulas for Shallow Water Correction of Propeller and Rudder Parameters

Empirical Formula for Shallow Water Correction of Propeller and Rudder Parameters as per Amin and Hasegawa [41].

$$\frac{(1-t_P)_{\text{Shallow}}}{(1-t_P)_{\text{Deep}}} = 1 + \begin{pmatrix} 29.495 - 14.089\dfrac{C_B L}{B} \\ +1.6486\left(\dfrac{C_B L}{B}\right)^2 \end{pmatrix}\begin{pmatrix} 0.004 - 0.035\dfrac{T}{h} \\ -0.104\left(\dfrac{T}{h}\right)^2 \end{pmatrix} \quad \text{(C1)}$$

$$\frac{\kappa_{\text{Shallow}}}{\kappa_{\text{Deep}}} = \begin{cases} 1 + \begin{pmatrix} 1220.41 - 396.037\,L/B \\ +31.676(L/B)^2 \end{pmatrix}(T/h)^{3.56} & \text{at } \dfrac{T}{h} \le -0.204\dfrac{L}{B} + 1.930 \\ 1 + \left(212.225 - 30.003\,C_B L/T + 1.017\left(C_B L/T\right)^2\right) & \text{at } \dfrac{T}{h} > -0.204\dfrac{L}{B} + 1.930 \\ \left(-0.139 + 1.002\,T/h - 0.757(T/h)^2\right) & \end{cases} \quad \text{(C2)}$$

$$\frac{\gamma_{\text{RShallow}}}{\gamma_{\text{RDeep}}} = \begin{cases} 1 + \begin{pmatrix} -135.247 + 2432.95\,C_B B/L \\ -10137.7\left(C_B B/L\right)^2 \end{pmatrix}(T/h)^{4.81} & \text{at } \dfrac{T}{h} \le -0.332\dfrac{T}{B} + 0.581 \\ 1 + \begin{pmatrix} -10.258 + 178.207\,C_B B/L \\ -686.249\left(C_B B/L\right)^2 \end{pmatrix}\begin{pmatrix} -3.854 + 13.665\,T/h \\ -10.468(T/h)^2 \end{pmatrix} & \text{at } \dfrac{T}{h} > -0.332\dfrac{T}{B} + 0.581 \end{cases} \quad \text{(C3)}$$

$$\frac{w_{\text{pShallow}}}{w_{\text{pdeep}}} = 1 + \left(-4.932 + 0.6425\,C_B L/T - 0.0165\left(C_B L/T\right)^2\right)(T/h)^{1.655} \quad \text{(C4)}$$

APPENDIX D: Supplementary Material

Table D1 Fujiwara geometry parameters

Parameter	Symbol	Value
Length	(L)	325.5 m
Breadth	(B)	58 m
Frontal projected area	(A_F)	1056 m²
Lateral projected area	(A_L)	4524.2 m²
Above-water projected area	(A_{OD})	675 m²
Distance from midship to center of lateral projected area	(C)	−13.3 m
Distance from midship to center of the Ass	(C_{BR})	−116 m
Height of superstructure	(H_{BR})	30.5 m
Height to the center of lateral projected area	(H_C)	8.34 m

Table D2 Propeller revolution

Condition	Ship speed	Propeller revolution
Full speed	15.5 kn	≈70 rpm
75 % speed	11.625 kn	≈53 rpm

Table D3 Rigid-body parameters

Parameter	Symbol	Value	Unit
Mass	(m)	312,622,000	kg
Radius of gyration	k_{zz}	80	m
Longitudinal centre of gravity	(x_G)	11.136	m

Table D4 The hydrodynamic coefficients related to the propeller and rudder for the simulation in deep water condition

Parameter	Value	Parameter	Value
t_p	0.220	x'_H	−0.464
k_2	−0.1385	f_α	2.747
k_1	−0.2753	ε	1.09
k_0	0.2931	κ	0.50
w_P	0.35	$\gamma_R(\beta_R<0)$	0.395
t_R	0.387	$\gamma_R(\beta_R>0)$	0.640
a_H	0.312		

Table D5 The correction of hydrodynamic coefficients related to the propeller and rudder for the simulation in shallow-water conditions

Parameters	Deep water	h/T=3	h/T=1.5	h/T =1.2
t_P	0.220	0.21186	0.19224	0.17875
κ	0.5	0.49594	0.45209	0.18249
$\gamma_R(\beta_R<0)$	0.395	0.40188	0.66050	0.51116
$\gamma_R(\beta_R>0)$	0.640	0.65114	1.07018	0.82820
w_P	0.35	0.37910	0.44165	0.48259

Table D6 Hydrodynamic derivatives in deep and shallow water conditions

Derivatives	Deep water	h/T=3.0	h/T=1.5	h/T=1.2
$X_{\dot{u}}$	17209142.95	21304262.19	42037303.28	98917514.02
$N_{\dot{r}}$	−2696727129955.26	−3475183838125.81	−5122910705177.66	−7839939596413.66
$N_{\dot{v}}$	−6665206191	−7172463932	−11597547307	−22289414050
$Y_{\dot{v}}$	−259623051.6	−348232676	−535788974.6	−845061034.4
$Y_{\dot{r}}$	−6665206191	−7172463932	−11597547307	−22289414050
X'_{vv}	−0.000725766	−0.000780477	−0.00134168	−0.002727383
X'_{vvvv}	0.007754013	0.008338544	0.014334388	0.029139105
X'_{rr}	−0.000334545	−0.000351358	−0.000523818	−0.000949648
X'_{vr}	−0.002428737	−0.002519414	−0.003574037	−0.006220472
Y'_{v}	−0.025265081	−0.02802116	−0.051324745	−0.106457578
Y'_{vvv}	−0.041378428	−0.044497716	−0.076493874	−0.155497603
Y'_{r}	0.004934964	0.00426099	0.005782887	0.007743289
Y'_{rrr}	−0.000381103	−0.00040272	−0.000611971	−0.001125273
Y'_{vvr}	−0.013927931	−0.01497788	−0.02574775	−0.052340314
Y'_{vrr}	−0.026352345	−0.028338901	−0.048716035	−0.099030502
N'_{v}	−0.008707238	−0.009918648	−0.018579601	−0.038907553
N'_{vvv}	−0.001197269	−0.001287524	−0.002213321	−0.004499264
N'_{r}	−0.003048687	−0.002827934	−0.003681418	−0.005952401
N'_{rrr}	−0.001254297	−0.001325441	−0.002014135	−0.003703525
N'_{vvr}	−0.008969989	−0.009194159	−0.007358461	−0.008511924
N'_{vrr}	0.00619069	0.002500748	0.006235665	0.022366016

Indices for various wind conditions

Table D7 Headwind scenarios

Indices	Cases	Wind speeds			
		5	10	15	20
Yaw rate	(full) h/T=1.2	−0.4588	−0.4581	−0.4568	−0.4549
	(full) h/T =1.5	−0.3890	−0.3870	−0.3836	−0.3787
	(full) h/T =3	−0.3528	−0.3504	−0.3462	−0.3404
	(75 %) h/T =1.2	−0.4625	−0.4611	−0.4588	−0.4551
	(75 %) h/T =1.5	−0.3910	−0.3874	−0.3813	−0.3726
	(75 %) h/T =3	−0.3526	−0.3482	−0.3409	−0.3303
Drift angle	(full) h/T =1.2	2.516	2.546	2.599	2.679
	(full) h/T =1.5	6.071	6.114	6.188	6.301
	(full) h/T =3	16.901	17.052	17.321	17.733
	(75 %) h/T =1.2	2.537	2.592	2.691	2.850
	(75 %) h/T =1.5	6.095	6.172	6.312	6.535
	(75 %) h/T =3	16.958	17.232	17.743	18.597
Speed change	(full) h/T =1.2	0.6730	0.6643	0.6497	0.6290
	(full) h/T =1.5	0.6074	0.5995	0.5862	0.5674
	(full) h/T =3	0.4122	0.4057	0.3948	0.3792
	(75 %) h/T =1.2	0.6708	0.6554	0.6294	0.5921
	(75 %) h/T =1.5	0.6061	0.5922	0.5685	0.5345
	(75 %) h/T =3	0.4115	0.4000	0.3804	0.3523

Table D8 Oblique headwind scenarios

Indices	Cases	Same direction of ship turning				Opposite direction of ship turning			
		Wind speeds				Wind speeds			
		5	10	15	20	5	10	15	20
Yaw rate	(full) h/T=1.2	−0.4610	−0.4665	−0.4753	−0.4866	−0.4570	−0.4504	−0.4391	−0.4225
	(full) h/T =1.5	−0.3900	−0.3909	−0.3921	−0.3933	−0.3887	−0.3858	−0.3806	−0.3730
	(full) h/T =3	−0.3526	−0.3494	−0.3438	−0.3356	−0.3539	−0.3548	−0.3561	−0.3578
	(75 %) h/T =1.2	−0.4663	−0.4758	−0.4903	−0.5075	−0.4592	−0.4474	−0.4266	−0.3944
	(75 %) h/T =1.5	−0.3928	−0.3942	−0.3958	−0.3963	−0.3905	−0.3852	−0.3756	−0.3607
	(75 %) h/T =3	−0.3522	−0.3464	−0.3361	−0.3209	−0.3545	−0.3560	−0.3582	−0.3607
Drift angle	(full) h/T =1.2	2.54	2.66	2.85	3.14	2.48	2.39	2.25	2.04
	(full) h/T =1.5	6.12	6.32	6.67	7.20	6.00	5.85	5.58	5.19
	(full) h/T =3	17.08	17.80	19.10	21.12	16.67	16.12	15.22	13.97
	(75 %) h/T =1.2	2.59	2.79	3.14	3.68	2.47	2.32	2.05	1.65
	(75 %) h/T =1.5	6.19	6.55	7.20	8.22	5.98	5.69	5.21	4.50
	(75 %) h/T =3	17.28	18.60	21.10	25.27	16.55	15.59	14.01	11.90
Speed change	(full) h/T =1.2	0.6735	0.6661	0.6540	0.6373	0.6756	0.6747	0.6734	0.6716
	(full) h/T =1.5	0.6074	0.5995	0.5865	0.5684	0.6101	0.6105	0.6113	0.6125
	(full) h/T =3	0.4116	0.4033	0.3897	0.3714	0.4151	0.4174	0.4214	0.4276
	(75 %) h/T =1.2	0.6716	0.6588	0.6378	0.6092	0.6754	0.6739	0.6716	0.6689
	(75 %) h/T =1.5	0.6061	0.5923	0.5695	0.5380	0.6109	0.6117	0.6132	0.6158
	(75 %) h/T =3	0.4104	0.3959	0.3726	0.3425	0.4166	0.4208	0.4284	0.4406

Table D9 Beam wind scenarios (90°)

Indices	Cases	Same direction of ship turning				Opposite direction of ship turning			
		Wind speeds				Wind speeds			
		5	10	15	20	5	10	15	20
Yaw rate	(full) h/T =1.2	−0.4631	−0.4747	−0.4929	−0.5162	−0.4551	−0.4426	−0.4204	−0.3863
	(full) h/T =1.5	−0.3914	−0.3963	−0.4039	−0.4135	−0.3880	−0.3825	−0.3727	−0.3571
	(full) h/T =3	−0.3537	−0.3535	−0.3529	−0.3514	−0.3537	−0.3535	−0.3527	−0.3503
	(75 %) h/T =1.2	−0.4700	−0.4899	−0.5198	−0.5558	−0.4558	−0.4330	−0.3906	−0.3204
	(75 %) h/T =1.5	−0.3953	−0.4037	−0.4159	−0.4301	−0.3891	−0.3791	−0.3598	−0.3254
	(75 %) h/T =3	−0.3540	−0.3536	−0.3518	−0.3481	−0.3540	−0.3534	−0.3508	−0.3424
Drift angle	(full) h/T =1.2	2.55	2.69	2.93	3.26	2.46	2.32	2.08	1.75
	(full) h/T =1.5	6.14	6.39	6.80	7.39	5.97	5.73	5.32	4.74
	(full) h/T =3	17.14	18.01	19.53	21.83	16.57	15.76	14.46	12.78
	(75 %) h/T =1.2	2.60	2.85	3.27	3.85	2.44	2.19	1.76	1.16
	(75 %) h/T T=1.5	6.22	6.65	7.40	8.47	5.93	5.49	4.77	3.72
	(75 %) h/T =3	17.37	18.94	21.80	26.26	16.38	14.98	12.83	10.18
Speed change	(full) h/T =1.2	0.6737	0.6673	0.6568	0.6427	0.6781	0.6847	0.6958	0.7116
	(full) h/T=1.5	0.6076	0.6005	0.5891	0.5736	0.6124	0.6196	0.6321	0.6502
	(full) h/T =3	0.4114	0.4027	0.3888	0.3706	0.4173	0.4264	0.4422	0.4656
	(75 %) h/T =1.2	0.6721	0.6609	0.6431	0.6200	0.6797	0.6914	0.7112	0.7387
	(75 %) h/T =1.5	0.6065	0.5943	0.5747	0.5490	0.6149	0.6279	0.6505	0.6844
	(75%) h/T =3	0.4101	0.3950	0.3719	0.3433	0.4205	0.4369	0.4661	0.5108

Table D10 Aft quartering wind scenarios

Indices	Cases	Same direction of ship turning				Opposite direction of ship turning			
		Wind speeds				Wind speeds			
		5	10	15	20	5	10	15	20
Yaw rate	(full) h/T =1.2	−0.4638	−0.4777	−0.4997	−0.5286	−0.4548	−0.4415	−0.4177	−0.3812
	(full) h/T =1.5	−0.3925	−0.4008	−0.4140	−0.4313	−0.3882	−0.3834	−0.3745	−0.3600
	(full) h/T =3	−0.3552	−0.3596	−0.3666	−0.3758	−0.3538	−0.3539	−0.3535	−0.3515
	(75 %) h/T =1.2	−0.4713	−0.4953	−0.5322	−0.5789	−0.4553	−0.4309	−0.3855	−0.3122
	(75 %) h/T=1.5	−0.3972	−0.4116	−0.4338	−0.4619	−0.3895	−0.3806	−0.3626	−0.3298
	(75 %) h/T =3	−0.3567	−0.3643	−0.3760	−0.3909	−0.3542	−0.3541	−0.3519	−0.3442
Drift angle	(full) h/T =1.2	2.54	2.64	2.79	2.99	2.45	2.30	2.05	1.71
	(full) h/T =1.5	6.12	6.29	6.57	6.92	5.97	5.71	5.30	4.74
	(full) h/T =3	17.05	17.64	18.59	19.87	16.56	15.72	14.44	12.86
	(75 %) h/T =1.2	2.58	2.75	3.00	3.32	2.43	2.15	1.73	1.19
	(75 %) h/T =1.5	6.17	6.47	6.93	7.49	5.92	5.47	4.76	3.82
	(75 %) h/T =3	17.22	18.24	19.87	21.97	16.36	14.94	12.90	10.56
Speed change	(full) h/T =1.2	0.6764	0.6778	0.6802	0.6838	0.6813	0.6973	0.7239	0.7603
	(full) h/T =1.5	0.6101	0.6106	0.6116	0.6134	0.6151	0.6306	0.6567	0.6936
	(full) h/T =3	0.4135	0.4110	0.4072	0.4028	0.4196	0.4355	0.4626	0.5016
	(75 %) h/T =1.2	0.6767	0.6792	0.6837	0.6907	0.6853	0.7135	0.7594	0.8201
	(75 %) h/T =1.5	0.6110	0.6119	0.6142	0.6183	0.6198	0.6472	0.6934	0.7595
	(75 %) h/T =3	0.4137	0.4096	0.4038	0.3979	0.4205	0.4369	0.4661	0.5108

Table D11 Following wind scenarios (180°)

Indices	Cases	Wind speeds			
		5	10	15	20
Yaw rate	(full) h/T =1.2	−0.4595	−0.4606	−0.4624	−0.4647
	(full) h/T =1.5	−0.3907	−0.3938	−0.3988	−0.4057
	(full) h/T =3	−0.3549	−0.3586	−0.3647	−0.3730
	(75 %) h/T =1.2	−0.4636	−0.4656	−0.4686	−0.4725
	(75 %) h/T =1.5	−0.3941	−0.3994	−0.4081	−0.4200
	(75 %) h/T =3	−0.3562	−0.3627	−0.3732	−0.3875
Drift angle	(full) h/T =1.2	2.49	2.45	2.38	2.29
	(full) h/T =1.5	6.04	5.98	5.88	5.76
	(full) h/T =3	16.78	16.57	16.25	15.84
	(75 %) h/T =1.2	2.49	2.42	2.31	2.18
	(75 %) h/T =1.5	6.03	5.93	5.77	5.59
	(75 %) h/T =3	16.74	16.39	15.87	15.28
Speed change	(full) h/T =1.2	0.6803	0.6934	0.7149	0.7444
	(full) h/T=1.5	0.6140	0.6258	0.6452	0.6719
	(full) h/T=3	0.4176	0.4274	0.4434	0.4653
	(75 %) h/T=1.2	0.6836	0.7064	0.7436	0.7939
	(75 %) h/T=1.5	0.6177	0.6384	0.6721	0.7176
	(75 %) h/T=3	0.4210	0.4381	0.4658	0.5032

REFERENCES

[1] Kim, D., Song, S., Jeong, B., Tezdogan, T., 2021. Numerical evaluation of a ship's manoeuvrability and course keeping control under various wave conditions using CFD. *Ocean Engineering*, 237, 109615. https://doi.org/10.1016/j.oceaneng.2021.109615

[2] Halder, P., Liu, S., 2025. Numerical investigation of added resistance of a container ship in short regular waves using unsteady RANS simulations. *Brodogradnja*, 76(2), 76204. https://doi.org/10.21278/brod76204

[3] Phuong, N. H., Taniguchi, T., Katayama, T., 2025. Numerical study of scale effects of viscous roll damping for a container ship. *Brodogradnja*, 76(4), 76406. https://doi.org/10.21278/brod76406

[4] Atasayan, E., Milanov, E., Alkan, A. D., 2024. Application of an offline grey box method for predicting the manoeuvring performance. *Brodogradnja*, 75(3), 75304. https://doi.org/10.21278/brod75304

[5] El Moctar, O., Sprenger, F., Schellin, T. E., Papanikolaou, A., 2016. Numerical and experimental investigations of ship maneuvers in waves. *35th International Conference on Ocean Offshore and Arctic Engineering*, 19-24 June, Busan, South Korea. https://doi.org/10.1115/omae2016-54847

[6] Hasnan, M. A. A., Yasukawa, H., Hirata, N., Terada, D., Matsuda, A., 2020. Study of ship turning in irregular waves. *Journal of Marine Science and Technology*, 25(4), 1024-1043. https://doi.org/10.1007/s00773-019-00698-1

[7] Sutulo, S., Guedes Soares, C., 2021. Review on ship manoeuvrability criteria and standards. Jou*rnal of Marine Science and Engineering*, 9(8), 904. https://doi.org/10.3390/jmse9080904

[8] Boviatsis, M., 2022. M/V EVER GIVEN: legal assessment of the causes and consequences of the accident. *WIT Transactions on the Built Environment*, 212, 185-196. https://doi.org/10.2495/UMT220161

[9] Xiao, F., 2014. Ships in an artificial force field: a multi-agent system for nautical traffic and safety. *Doctoral Thesis*, Delft University of Technology. https://doi.org/10.4233/uuid:879d6d69-2c2f-45e7-beb1-a3c1fd1d035c

[10] Du, P., Ouahsine, A., Toan, K. T., Sergent, P., 2018. Simulation of ship maneuvering in a confined waterway using a nonlinear model based on optimization techniques. *Ocean Engineering*, 142, 194-203. https://doi.org/10.1016/j.oceaneng.2017.07.013

[11] Gadelho, J. F. M., Rodrigues, J. M., Lavrov, A., Guedes Soares, C., 2018. Heave and sway hydrodynamic coefficients of ship hull sections in deep and shallow water using Navier-Stokes equations. *Ocean Engineering*, 154, 262-276. https://doi.org/10.1016/j.oceaneng.2018.02.025

[12] Liu, Y., Li, B., Zou, Z. J., 2019. Manoeuvrability prediction for container ships in deep and shallow waters. *Journal of Ship Mechanics*, 23, 267-282. 10.3969/j.issn.1007-7294.2019.03.003

[13] Li, J., Wang, Q., Dong, K., Wang, X., 2024. Numerical simulations of a ship's maneuverability in shallow water. *Journal of Marine Science and Engineering*, 12(7), 1076. https://doi.org/10.3390/jmse12071076

[14] Carrica, P. M., Mofidi, A., Eloot, K., Delefortrie, G., 2016. Direct simulation and experimental study of zigzag maneuver of KCS in shallow water. *Ocean Engineering*, 112, 117-133. https://doi.org/10.1016/j.oceaneng.2015.12.008

[15] Kim, D., Kim, S. H., Kim, S. J., Paik, K. J., 2017. A study on the sensitivity analysis of the hydrodynamic derivatives on the maneuverability of KVLCC2 in shallow water. *Brodogradnja*, 68(4), 1-22. https://doi.org/10.21278/brod68401

[16] Inoue, S., Hirano, M., Hirakawa, Y., Mukai, K., 1979. The hydrodynamic derivative on ship maneuverability in even keel condition. *Transactions of the West Japan Society of Naval Architects*, 57.

[17] Wang, Y., Du, W., Li, G., Li, Z., Hou, J., Hu, H., 2022. Efficient ship maneuvering prediction with wind, wave and current Effects. *Advances in Transdisciplinary Engineering*. https://doi.org/10.3233/ATDE220115

[18] Sukas, O. F., Kinaci, O. K., Bal, S., 2019. Theoretical background and application of MANSIM for ship maneuvering simulations. *Ocean Engineering*, 192, 106239. https://doi.org/10.1016/j.oceaneng.2019.106239

[19] Taimuri, G., Matusiak, J., Mikkola, T., Kujala, P., Hirdaris, S., 2020. A 6-DoF maneuvering model for the rapid estimation of hydrodynamic actions in deep and shallow waters. *Ocean Engineering*, 218, 108103. https://doi.org/10.1016/j.oceaneng.2020.108103

[20] Kostoulas, C., 2017. Container vessel maneuvering model in shallow waters and assessment of maneuvering coefficients through system identification. *Master's Thesis*, KTH Royal Institute of Technology, School of Architecture and the Built Environment.

[21] Tang, X., Tong, S., Huang, G., Xu, G., 2020. Numerical investigation of the maneuverability of ships advancing in the non-uniform flow and shallow water areas. *Ocean Engineering*, 195, 106679. https://doi.org/10.1016/j.oceaneng.2019.106679

[22] Novaselic, M., Mohovic, R., Baric, M., Grbić, L., 2021. Wind influence on ship manoeuvrability–a turning circle analysis. *TransNav: International Journal on Marine Navigation and Safety of Sea Transportation*, 15(1), 47-51. https://doi.org/10.12716/1001.15.01.03

[23] Zhu, M., Wang, T., Zhang, H., Li, G., 2022. Ship manoeuvring model identification under wind disturbance. *International Conference on Real-time Computing and Robotics* (RCAR), 17-22 July, Guiyang, China, 648-653. https://doi.org/10.1109/RCAR54675.2022.9872289

[24] Wang, T., Li, G., Wu, B., Æsøy, V., Zhang, H., 2021. Parameter identification of ship manoeuvring model under disturbance using support vector machine method. S*hips and Offshore Structures*, 16(sup1), 13-21. https://doi.org/10.1080/17445302.2021.1927600

[25] Huang, J. C., Nieh, C. Y., Kuo, H. C., 2019. Risk assessment of ships maneuvering in an approaching channel based on AIS data. *Ocean Engineering*, 173, 399-414. https://doi.org/10.1016/j.oceaneng.2018.12.058

[26] Zhu, M., 2021. Genetic algorithm-based parameter identification for ship manoeuvring model under wind disturbance. *Master's Thesis*, NTNU. https://hdl.handle.net/11250/2824237

[27] Yasukawa, H., Hirono, T., Nakayama, Y., Koh, K. K., 2012. Course stability and yaw motion of a ship in steady wind. *Journal of Marine Science and Technology*, 17, 291-304. https://doi.org/10.1007/s00773-012-0168-z

[28] Yasukawa, H., Yoshimura, Y., 2015. Introduction of MMG standard method for ship maneuvering predictions. *Journal of Marine Science and Technology*, 20(1), 37-52. https://doi.org/10.1007/s00773-014-0293-y

[29] Brix, J. E., 1993. Manoeuvring Technical Manual. *Seehafen-Verl.,* Hamburg.

[30] Clarke, D., Gedling, P., Hine, G., 1982. The application of manoeuvring criteria in hull design using linear theory. *Royal Institute of Navigation Architecture*, 45-68.

[31] Raven, H. C., 2016. A new correction procedure for shallow-water effects in ship speed trials. *Proceedings of the 13th International Symposium on Practical Design of Ships and Other Floating Structures*, 4-8 September, Copenhagen, Denmark.

[32] ITTC., 2017b. Preparation, conduct and analysis of speed/power trials. Appendix K, Raven Shallow Water Correction. *ITTC Recommended Proceedings*, 7.5-04-01-01.1, Revision 5, Guidel, France, 71-73.

[33] Yoshimura, Y., Masumoto, Y., 2011. Hydrodynamic force database with medium high speed merchant ships including fishing vessels and investigation into a manoeuvring prediction method. *Journal of the Japan Society of Naval Architects and Ocean* Engineers, 14, 63-73. https://doi.org/10.2534/jjasnaoe.14.63

[34] Lee, H. Y., Shin, S. S., 1998. The prediction of ship's manoeuvring performance in initial design stage. *Developments in Marine Technology*, 11, 633-639. https://doi.org/10.1016/S0928-2009(98)80205-9

[35] Kijima, K., Katsuno, T., Nakiri, Y., Furukawa, Y., 1990a. On the manoeuvring performance of a ship with the parameter of loading condition. *Journal of the Society of Naval Architects of Japan*, 168, 141-148. https://doi.org/10.2534/jjasnaoe1968.1990.168_141

[36] Norrbin, N. H., 1970. Theory and observation on the use of a mathematical model for ship maneuvering in deep and confined waters. *Proceedings of the 8th Symposium on Naval Hydrodynamics*, 24-28 August, Rome, Italy.

[37] Khattab, O., 1984. Multiple regression analysis of the hydrodynamic derivatives for manoeuvring equations, *BSRA*, Report W1090.

[38] Ankudinov, V. K., Miller, E. R., Jakobsen, B. K., Daggett, L. L., 1990. Manoeuvring performance of tug/barge assemblies in restricted waterways. *Proceedings of International Conference on Marine Simulation and Ship Maneuverability* (MARSIM & ICMS), 515-525.

[39] Li, M. J., Wu, X. H., 1990. Simulation calculation and comprehensive assessment on ship maneuverabilities in wind, wave, current and shallow water. *Journal of Hydrodynamics*, 4, 59-72.

[40] Vantorre, M., 2001. Manoeuvring coefficients for a container carrier in shallow water: an evaluation of semi-empirical formulae. *Mini Symposium on Prediction of Ship Manoeuvring Performance*, 18 October, Tokyo, Japan, 71-81.

[41] Amin, O. M., Hasegawa, K., 2010. Generalized mathematical model for ship manoeuvrability considering shallow water effect. *Conference Proceedings of Japan Society of Naval Architects and Ocean Engineers*, 10, 531-534.

[42] Fujiwara, T., Ueno, M., Nimura, T., 1998. Estimation of wind forces and moments acting on ships. *Journal of the Society of Naval Architects of Japan*, 183, 77-90. https://doi.org/10.2534/jjasnaoe1968.1998.77

[43] ITTC., 2021. Quality system manual: recommended procedures and guidelines: preparation, conduct and analysis of speed/power trials. Available online: https://www.ittc.info/media/9874/75-04-01-011.pdf (accessed 18th August 2024)

[44] SIMMAN, 2020. Workshop on verification and validation of ship manoeuvring simulation methods. https://www.simman2020.kr/ (accessed 23rd January 2025)

[45] Morris, M. D., 1991. Factorial sampling plans for preliminary computational experiments. *Technometrics*, 33(2), 161-174.

[46] Saltelli, A., Ratto, M., Andres, T., Campolongo, F., Cariboni, J., Gatelli, D., Saisana, M., Tarantola, S., 2008. Global sensitivity analysis: the primer. *John Wiley & Sons: Hoboken*, NJ, USA. https://doi.org/10.1002/9780470725184

[47] Efron, B., Tibshirani, R. J., 1994. An introduction to the bootstrap (1st ed.). *Chapman and Hall/CRC*. https://doi.org/10.1201/9780429246593

[48] Shapiro, S. S., Wilk, M. B., 1965. An analysis of variance test for normality (complete samples). *Biometrika*, 52(3-4), 591-611. https://doi.org/10.1093/biomet/52.3-4.591